


# Mirror Optical Activity: Nanophotonic Chiral Sensing from Parity Indefiniteness

A. Ciattoni<sup>1</sup>\*

CNR-SPIN, c/o Dip.to di Scienze Fisiche e Chimiche, Via Vetoio, Coppito, L'Aquila 67100, Italy

 (Received 27 July 2021; revised 6 September 2021; accepted 9 September 2021; published 23 September 2021)

Mirror symmetry is among the most fundamental concepts of physics, and its spontaneous breaking at the molecular level allows chiral molecules to exist in two enantiomers that are mirror images of each other. The majority of the chiro-optical effects routinely used to detect enantiomers in mixtures, such as circular dichroism, rely on chiral sensitivity to photon circular polarization, and thus do not harness the full potential of mirror-symmetry breaking, which also involves the spatial profile of the radiation. Here we show that the parity indefiniteness of an electromagnetic field interacting with chiral matter supports mirror optical activity, a chiro-optical effect where a chiral film, when it is probed by the mirror-symmetric field of a nanoemitter, produces a near field whose spatial profile has broken mirror symmetry. The detection of near-field dissymmetry can provide an efficient chiral sensing technique. We specialize the discussion to nanofilms with infrared chirality by using a swift electron in an aloof configuration as the nanoemitter and an off-axis transparent conducting nanoparticle as the near-field probe; the spatial dissymmetry factor of the nanoparticle cathodoluminescence is 1 order of magnitude larger than the dimensionless circular dichroism, and is further enhanced to 2 orders of magnitude if an additional graphene sheet is deposited on the film interface.

DOI: [10.1103/PhysRevApplied.16.034041](https://doi.org/10.1103/PhysRevApplied.16.034041)

## I. INTRODUCTION

Explicit symmetry breaking, the artificial lowering of the symmetry group of a system, is a ubiquitous and key physical concept, since it creates phenomena characterized by intriguing asymmetric behavior, as first clarified by Pierre Curie in 1894 [1]. For example, if time reversal is broken, photonic crystals with Dirac points display topological properties [2,3] and support topologically protected photonic edge modes with unidirectional propagation [4]. Besides, the interplay of parity and time-reversal breaking in  $PT$ -symmetric photonic systems [5] underpins unidirectional reflectionless propagation in periodic structures [6] and angular-momentum vortex lasing in microrings [7]. Chiral phenomena involve only parity breaking and are of fundamental interest in physics, with important implications for biology and the life sciences. Molecular chirality, resulting microscopically from spontaneous parity breaking, explicitly breaks mirror symmetry at the macroscopic scale and, accordingly, even homogeneous and isotropic chiral matter displays optical activity [8], i.e., an asymmetric interaction with left and right circularly polarized photons. Such asymmetry enables chiro-sensitive molecular detection through circular dichroism (the differential absorption of left and right circularly polarized light) or optical rotation (rotation of the polarization

plane of light produced by a chiral medium), which is highly relevant in biological chemistry and pharmacology, since many organic molecules are chiral. However, the mismatch between the molecular size and the radiation wavelength severely limits the strength of chiro-optical phenomena and, accordingly, a number of strategies have been proposed to achieve enhanced chiral sensing [9–11]. Paradigmatic examples are plasmon-enhancement circular dichroism [12–15], which exploits near-field effects to reduce the molecular-field spatial-scale mismatch, and the use of superchiral fields, where a local enhancement of optical chirality [16,17] amplifies the differential circular-dichroism signal [18–20], both in plasmonic [21–24] and in dielectric [25–28] setups. Other ingenious chiral sensing techniques have also been conceived that use femtosecond spectroscopy [29], photoionization [30,31], and signal-reversing cavity ringdown polarimetry [32].

Nearly all the chiro-optical phenomena hitherto considered rely on the effect of chiral matter on the polarization of light, as in optical rotation, or on a comparison of the response of a medium to two excitations of opposite polarization handedness, as in circular dichroism. However, the geometric operation of spatial reflection, in addition to changing the direction of the electric (vector) and magnetic (pseudovector) fields, also involves the specular inversion of their profiles, and the question arises as to whether explicit mirror-symmetry breaking is able to create chiro-optical effects displaying asymmetric spatial

\*alessandro.ciattoni@spin.cnr.it

features. Here, we answer this question affirmatively by demonstrating theoretically that a mirror-symmetric field (i.e., spatially coinciding with its mirror image) is reflected and transmitted by a chiral film into fields with indefinite parity, a phenomenon we refer to as mirror optical activity (MOA). The spatial asymmetry of the reflected and transmitted fields is a consequence of the fundamental electromagnetic parity indefiniteness in chiral media and is such that two geometrically identical samples, with opposite chirality (enantiomers) and excited by the same probe, produce fields that are mirror images of each other. Since any chiro-optical effect is magnified by near-field interactions, MOA induced by a nanoemitter is particularly marked, and the detection of the near-field asymmetry provides an efficient technique for enantiomeric discrimination. We specialize our general reasoning to a chiral molecular layer, with the possible inclusion of a graphene sheet at its interface, interacting with a fast electron in an aloof configuration, and we probe MOA through a transparent semiconducting nanoparticle, whose position-dependent cathodoluminescence emission provides evidence of near-field asymmetry and chiral sensing.

## II. ELECTROMAGNETIC PARITY INDEFINITENESS

The starting point of our analysis is reflection invariance, which states that when a complete experiment is subjected to mirror reflection, the resulting experiment should, in principle, be realizable (when the weak interaction can be neglected). In order to deal with an electromagnetic field

of complex amplitudes  $\mathbf{E}_\omega(\mathbf{r}), \mathbf{H}_\omega(\mathbf{r})$  (with a suppressed  $e^{-i\omega t}$  factor) existing in a homogeneous and isotropic chiral medium (see Appendix A), we consider the geometric reflection through a plane

$$\mathbf{r} \rightarrow \mathbf{r}' = \mathcal{R}\mathbf{r} \quad (1)$$

and the mirror image of the field

$$\begin{aligned} \mathbf{E}'_\omega(\mathbf{r}) &= \mathcal{R}\mathbf{E}_\omega(\mathcal{R}\mathbf{r}), \\ \mathbf{H}'_\omega(\mathbf{r}) &= -\mathcal{R}\mathbf{H}_\omega(\mathcal{R}\mathbf{r}), \end{aligned} \quad (2)$$

stemming from the vector and pseudovector natures of the electric and magnetic fields, respectively (where  $\mathcal{R}$  is the dyadic reversing the sign of the vector component normal to the plane). The mirror image of the medium is identical but with opposite chirality (the opposite enantiomeric medium), since microscopically each chiral molecule is reflected into its opposite enantiomer [see Fig. 1(a)]. Reflection invariance states that  $\mathbf{E}'_\omega, \mathbf{H}'_\omega$  is a physically admissible field in the opposite enantiomeric medium. In other words, if the field  $\mathbf{E}_\omega, \mathbf{H}_\omega$  satisfies the Maxwell equations with constitutive relations

$$\begin{aligned} \mathbf{D}_\omega &= \varepsilon_0\varepsilon\mathbf{E}_\omega - \frac{i}{c}\kappa\mathbf{H}_\omega, \\ \mathbf{B}_\omega &= \mu_0\mathbf{H}_\omega + \frac{i}{c}\kappa\mathbf{E}_\omega, \end{aligned} \quad (3)$$

where  $\varepsilon$  is the dielectric permittivity and  $\kappa$  is the Pasteur parameter accounting for the electromagnetic coupling

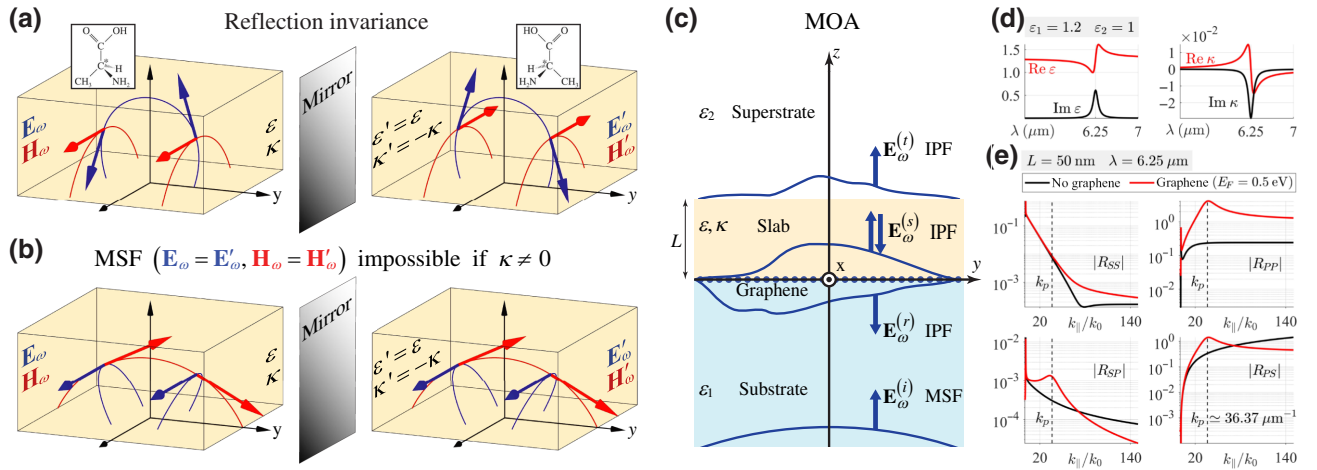


FIG. 1. Electromagnetic parity indefiniteness in chiral media and MOA. (a) If a field  $\mathbf{E}_\omega, \mathbf{H}_\omega$  exists in a homogeneous chiral medium, its mirror image  $\mathbf{E}'_\omega, \mathbf{H}'_\omega$  is a physically admissible field in the opposite enantiomeric medium. (b) A mirror-symmetric field (MSF) cannot exist in a chiral medium, since it should exist in the opposite enantiomeric medium as well. (c) MOA produced by a chiral slab sandwiched between two achiral dielectrics, with the potential inclusion of a graphene sheet. The incident (*i*) MSF triggers the excitation of an indefinite-parity field (IPF) in the slab (*s*), in turn producing reflected (*r*) and transmitted (*t*) IPFs. (d) Parameters of the setup used for numerical evaluations. (e) Reflection coefficients of a 50-nm-thick chiral slab at the molecular resonance  $\lambda = 6.25 \mu\text{m}$  as functions of the (normalized) transverse photon momentum, with and without graphene inclusion.

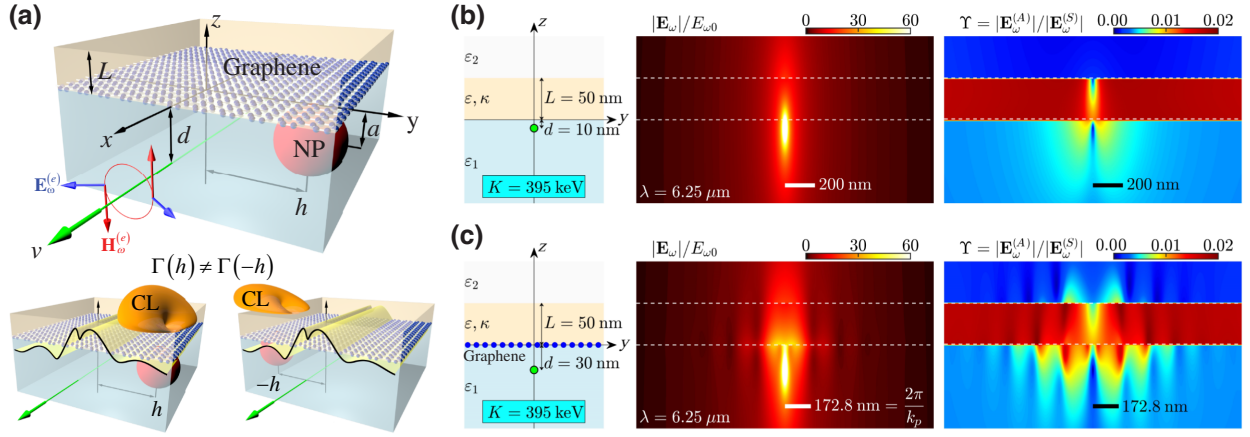


FIG. 2. MOA triggered by fast electrons. (a) A fast electron traveling at velocity  $v$  through a substrate in an alroof configuration generates a MSF triggering MOA, while an off-axis nanoparticle (NP) at  $y = h$  locally probes the near field. Because of the asymmetric near field (yellow), the cathodoluminescence (CL) emission probabilities  $\Gamma(h)$  and  $\Gamma(-h)$  of the nanoparticle when located at two mirror-symmetric positions are unequal, their difference providing MOA detection and chiral sensing. (b,c). Normalized modulus of the total field  $\mathbf{E}_\omega$  and its dissymmetry factor  $\Upsilon$  in two setups (without nanoparticle): (b) without graphene and (c) with inclusion of graphene.  $\Upsilon$  provides a local estimation of MOA efficiency.

produced by molecular chirality, the mirror-image field  $\mathbf{E}'_\omega, \mathbf{H}'_\omega$  satisfies the same Maxwell equations but with  $\varepsilon' = \varepsilon$  and  $\kappa' = -\kappa$ , as sketched in Fig. 1(a) (see Appendix B). This well-known fact has a direct consequence that seems to have been overlooked in the subject of chiro-optics: a mirror-symmetric field, i.e., a field coinciding with its mirror image  $\mathbf{E}_\omega = \mathbf{E}'_\omega, \mathbf{H}_\omega = \mathbf{H}'_\omega$ , cannot exist in a chiral medium, since it should be an admissible field also in the opposite enantiomeric medium [see Fig. 2(a)]. Evidently, the argument breaks down in the absence of chirality ( $\kappa = 0$ ), since an achiral medium coincides with its mirror image.

In order to thoroughly characterize the above dissymmetry, it is useful to focus on the electric field satisfying the equation

$$-\nabla \times \nabla \times \mathbf{E}_\omega + k_0^2 (\varepsilon - \kappa^2) \mathbf{E}_\omega = 2k_0\kappa \nabla \times \mathbf{E}_\omega, \quad (4)$$

where  $k_0 = \omega/c$ , which is fully equivalent to the Maxwell equations and whose explicit broken mirror symmetry is evident, since its lhs is a vector, whereas its rhs is a pseudovector scaled by the chirality parameter  $\kappa$ . Consider now the symmetric and antisymmetric parts of the electric field, given by

$$\begin{aligned} \mathbf{E}_\omega^S &= \frac{1}{2} (\mathbf{E}_\omega + \mathbf{E}'_\omega), \\ \mathbf{E}_\omega^A &= \frac{1}{2} (\mathbf{E}_\omega - \mathbf{E}'_\omega), \end{aligned} \quad (5)$$

which have definite parity, since they are eigenstates of the reflection operator  $\hat{R}$  acting on vector fields as  $\hat{R}[\mathbf{A}(\mathbf{r})] = \mathcal{R}\mathbf{A}(\mathcal{R}\mathbf{r})$ , with eigenvalues  $+1$  and  $-1$ , respectively. As a consequence,  $\mathbf{E}_\omega$  is a MSF or a mirror-antisymmetric

field (MAF) if  $\mathbf{E}_\omega^A = 0$  or  $\mathbf{E}_\omega^S = 0$ , respectively. Inserting the decomposition  $\mathbf{E}_\omega = \mathbf{E}_\omega^S + \mathbf{E}_\omega^A$  into Eq. (4) and separating the symmetric and antisymmetric parts of the resultant equation, we obtain

$$\begin{aligned} -\nabla \times \nabla \times \mathbf{E}_\omega^S + k_0^2 (\varepsilon - \kappa^2) \mathbf{E}_\omega^S &= 2k_0\kappa \nabla \times \mathbf{E}_\omega^A, \\ -\nabla \times \nabla \times \mathbf{E}_\omega^A + k_0^2 (\varepsilon - \kappa^2) \mathbf{E}_\omega^A &= 2k_0\kappa \nabla \times \mathbf{E}_\omega^S, \end{aligned} \quad (6)$$

which vividly show how chirality couples the definite-parity parts of the field. What is essential for our purposes is that these equations make it clear that  $\mathbf{E}_\omega^S$  and  $\mathbf{E}_\omega^A$  cannot separately vanish (unless the extremely critical condition  $\varepsilon = \kappa^2$  is achieved), thus showing that neither MSFs (as proven above) nor MAFs can exist in a chiral medium. We conclude that a field interacting with chiral matter is always an IPF, and this is the most comprehensive consequence of macroscopic explicit symmetry breaking produced by molecular chirality. It is worth emphasizing that in achiral media the symmetric and antisymmetric parts of the field are not coupled [see Eq. (6) with  $\kappa = 0$ ], and consequently MSFs, MAFs, and IPFs are all physically admissible fields.

### III. MIRROR OPTICAL ACTIVITY

The peculiarity of electromagnetic parity indefiniteness raises the question of what happens when a chiral sample surrounded by an achiral environment is probed by an external field with definite parity. Since the sample hosts only IPFs, it turns out that the field it produces in the environment cannot have definite parity, thus showing dissymmetric features. Such an asymmetric response to a symmetric stimulus is a chiro-optical effect, namely MOA, since it is entirely due to the sample chirality.

To prove these observations and make them quantitative, we consider a chiral slab ( $\varepsilon, \kappa$ ) surrounded by a substrate ( $\varepsilon_1$ ) and a superstrate ( $\varepsilon_2$ ) that are achiral transparent dielectrics, as sketched in Fig. 1(c). We also incorporate a graphene sheet lying at the slab-substrate interface since, although it is not essential for the onset of MOA, the excitation of plasmon polaritons combined with field dissymmetry triggers a near-field interferometric mechanism able to enhance enantiomeric sensing (see below). Because of its planar geometry and homogeneity, the setup is geometrically (but not physically) left invariant by reflections through any plane orthogonal to the interfaces, and so, to isolate asymmetric electromagnetic features entirely due to chirality, we focus hereafter on reflection through the  $xz$  plane, i.e.,  $\mathcal{R} = \mathbf{e}_x \mathbf{e}_x - \mathbf{e}_y \mathbf{e}_y + \mathbf{e}_z \mathbf{e}_z$ . The slab is probed by an incident MSF,  $\mathbf{E}_\omega^{(i)}(\mathbf{r}) = \mathcal{R} \mathbf{E}_\omega^{(i)}(\mathcal{R}\mathbf{r})$ , in the substrate, which is given in full generality by

$$\mathbf{E}_\omega^{(i)} = \int d^2 \mathbf{k}_\parallel e^{i\mathbf{k}_\parallel \cdot \mathbf{r}_\parallel} e^{ik_{1z}z} \left[ U_S^{(i)} \mathbf{u}_S + U_P^{(i)} \left( \mathbf{u}_P - \frac{k_\parallel}{k_{1z}} \mathbf{e}_z \right) \right], \quad (7)$$

where the subscript  $\parallel$  hereafter labels a vector parallel to the slab ( $\mathbf{A}_\parallel = A_x \mathbf{e}_x + A_y \mathbf{e}_y$ ),  $k_{1z} = \sqrt{k_0^2 \varepsilon_1 - k_\parallel^2}$ ,  $\mathbf{u}_S = \mathbf{e}_z \times \mathbf{k}_\parallel / k_\parallel$  and  $\mathbf{u}_P = \mathbf{k}_\parallel / k_\parallel$  are the transverse electric ( $S$ ) and transverse magnetic ( $P$ ) unit vectors in momentum space, and  $U_S^{(i)}$  and  $U_P^{(i)}$  are the corresponding amplitudes. The definite positive parity (+1) of the incident field amounts in momentum space to the antisymmetry and symmetry of its  $S$  and  $P$  amplitudes, respectively, i.e.,  $U_S^{(i)}(\mathbf{k}_\parallel) = -U_S^{(i)}(\mathcal{R}\mathbf{k}_\parallel)$ ,  $U_P^{(i)}(\mathbf{k}_\parallel) = U_P^{(i)}(\mathcal{R}\mathbf{k}_\parallel)$ . An IPF  $\mathbf{E}_\omega^{(s)}$  arises inside the slab together with reflected and transmitted fields  $\mathbf{E}_\omega^{(r)}$  and  $\mathbf{E}_\omega^{(t)}$  in the substrate and superstrate, respectively (see Secs. 1 and 2). To show that the reflected field (and, analogously, the transmitted field) is an IPF, we note that its symmetric and antisymmetric parts are

$$\begin{aligned} \mathbf{E}_\omega^{(r)S} &= \int d^2 \mathbf{k}_\parallel e^{i\mathbf{k}_\parallel \cdot \mathbf{r}_\parallel} e^{-ik_{1z}z} \\ &\quad \times \left[ R_{SS} U_S^{(i)} \mathbf{u}_S + R_{PP} U_P^{(i)} \left( \mathbf{u}_P + \frac{k_\parallel}{k_{1z}} \mathbf{e}_z \right) \right], \\ \mathbf{E}_\omega^{(r)A} &= n \int d^2 \mathbf{k}_\parallel e^{i\mathbf{k}_\parallel \cdot \mathbf{r}_\parallel} e^{-ik_{1z}z} \\ &\quad \times \left[ R_{SP} U_P^{(i)} \mathbf{u}_S + R_{PS} U_S^{(i)} \left( \mathbf{u}_P + \frac{k_\parallel}{k_{1z}} \mathbf{e}_z \right) \right], \quad (8) \end{aligned}$$

where  $n = \sqrt{\varepsilon \kappa^2} / \kappa$  and  $R_{ij}$  is the reflection coefficient providing the contribution to the  $i = \{S, P\}$  amplitude of the reflected field produced by the  $j = \{S, P\}$  amplitude of the incident field (see Sec. 3). Now  $\mathbf{E}_\omega^{(r)S}$  and  $\mathbf{E}_\omega^{(r)A}$  vanish only if  $U_S^{(i)}$  and  $U_P^{(i)}$  simultaneously vanish, i.e., only if

there is no incident field, thus proving that the reflected field is always an IPF. Remarkably,  $\mathbf{E}_\omega^{(r)A}$  contains only the mixing coefficients  $R_{SP}$  and  $R_{PS}$ , which vanish in the absence of chirality ( $\kappa = 0$ ), since in this case the  $S$  and  $P$  polarizations are independent. This shows that MOA, the emergence of an antisymmetric part of the field reflected by a homogeneous chiral slab probed by an incident MSF, is an effect entirely due to the slab chirality.

Another specific chiro-optical feature of MOA is that two slabs that are identical but filled with opposite enantiomeric media and probed by the same incident MSF produce reflected field that are mirror images of each other. Indeed, since the reflection coefficients  $R_{ij}$  are left invariant by the chirality reversal  $\kappa \rightarrow -\kappa$  (see Appendix C), the symmetric and antisymmetric parts of the field reflected by a slab with chirality  $-\kappa$  are  $\mathbf{E}_\omega^{(r)S}$  and  $-\mathbf{E}_\omega^{(r)A}$ , due to the  $n$  in the second equation of Eq. (8), and these are precisely the symmetric and antisymmetric parts of  $\mathbf{E}_\omega^{(r)}$ , the mirror image of the field reflected by a slab with chirality  $\kappa$ . Such a MOA feature suggests viable enantiomeric sensing techniques where the detection of the asymmetry of the reflected field enables the discrimination of different enantiomerically pure samples or the measurement of the enantiomeric excess of a mixture.

To discuss MOA in more depth, we focus on the reflection coefficients  $R_{ij}$  pertaining to a specific chiral slab of thickness  $L = 50$  nm lying on a dielectric substrate in vacuum [the electromagnetic parameters of the setup are detailed in Fig. 1(d)]. In view of the potential inclusion of graphene and its infrared effectiveness, we choose the chiral medium to be a dielectric matrix with dispersed molecules of  $\alpha$ -alanine, due to its marked chiral response resulting from a vibrational mode at  $1600 \text{ cm}^{-1}$  [33,34]. In Fig. 1(e), we plot the moduli of the reflection coefficients  $|R_{ij}(k_\parallel)|$  at the molecular resonance  $\lambda = 6.25 \text{ }\mu\text{m}$  as functions of the transverse photon momentum (its direction does not affect the coefficients, by isotropy; see Sec. 1) both without graphene (black curves) and with graphene of Fermi energy  $E_F = 0.5 \text{ eV}$  (red curves). In the graphene-free case, the most striking feature is that the relevant MOA coefficients  $R_{SP}$  and  $R_{PS}$  [see the second equation of Eq. (8)] display quite opposite behaviors at large photon momenta  $k_\parallel \gg k_0$ , the first being small and fading, the second increasing and reaching relatively large values, with  $|R_{PS}| \gg |R_{SP}|$ . Analogous behaviors are shown by the coefficients  $R_{SS}$  and  $R_{PP}$  ruling the symmetric part of the reflected field. Therefore the MOA is enhanced if it is triggered by an incident MSF with deep subwavelength spatial features, such as the field of a nanoemitter, whose photons are mainly  $S$  polarized since these traits highlight  $\mathbf{E}_\omega^{(r)A}$  at the expense of  $\mathbf{E}_\omega^{(r)S}$ . The qualitative behavior of the reflection coefficients is not altered by the inclusion of graphene, which basically yields a plasmon resonance peak at  $k_p \simeq 36.17k_0 = 36.37 \text{ }\mu\text{m}^{-1}$  (except for the purely  $S$  coefficient  $R_{SS}$ ).



Before delving into the analysis of a feasible scheme for observing MOA, we elucidate its underpinning electromagnetic mechanism to explain the behavior of the mixing reflection coefficients in momentum space. The key fact is that photons are circularly polarized in chiral media so that their  $S$  and  $P$  components are not independent (see Sec. 1), the corresponding  $S$ - $P$  effective coupling having three main relevant consequences. First, it is responsible for the mixing reflection processes described by the coefficients  $R_{SP}$  and  $R_{PS}$ , where incoming photons of one kind are reflected into photons of the other kind. Second, it makes such mixing reflection processes very sensitive also to the incoming magnetic field

$$\mathbf{H}_\omega^{(i)} = \frac{1}{Z_0} \int d^2 \mathbf{k}_\parallel e^{i \mathbf{k}_\parallel \cdot \mathbf{r}_\parallel} e^{i k_{1z} z} \times \left[ \frac{k_0 \varepsilon_1}{k_{1z}} U_P^{(i)} \mathbf{u}_S - \frac{k_{1z}}{k_0} U_S^{(i)} \left( \mathbf{u}_P - \frac{k_\parallel}{k_{1z}} \mathbf{e}_z \right) \right], \quad (9)$$

where  $Z_0 = \sqrt{\mu_0/\varepsilon_0}$ , due to the manifest  $S$ - $P$  role switch of its amplitudes. Third, it dramatically reduces the  $S$  component of large-momentum photons in the chiral slab, since their  $P$  and  $z$  components combine, by isotropy, into a nearly circularly polarized state for  $k_\parallel \gg k_0$  (the transverse spin of  $TM$  evanescent waves [35]), and the orthogonal  $S$  component is suppressed to preserve the photon circular polarization (see Sec. 1). Now the reflection process  $P \rightarrow S$  ( $U_S^{(i)} = 0$ ,  $U_P^{(i)} \neq 0$ ), where an incoming photon of kind  $P$  is reflected into a photon of kind  $S$ , is extremely inefficient for  $k_\parallel \gg k_0$ , since the magnetic field contribution is negligible (due to  $k_{1z} \simeq i k_\parallel$  in the denominator) and the field in the slab has a negligible  $S$  component, thus explaining the asymptotic falloff of  $R_{SP}$ . Conversely, the reflection process  $S \rightarrow P$  ( $U_S^{(i)} \neq 0$ ,  $U_P^{(i)} = 0$ ) is boosted for  $k_\parallel \gg k_0$ , since the magnetic field contribution is very large (due to  $k_{1z} \simeq i k_\parallel$  in the numerator) and the field in the slab is almost of  $P$  kind, thus explaining the dramatic enhancement of  $R_{PS}$  in the large-photon-momentum regime.

#### IV. MOA TRIGGERED BY FAST ELECTRONS

An electron traveling at relativistic speed is a very appropriate source for triggering MOA, since the cylindrically symmetric field it creates is a MSF with a strong near field. In addition, the electron velocity affects the inclination of the electric field vector, thus providing management of its  $S$ - $P$  content in momentum space, which is useful for MOA. For these reasons, we focus hereafter on the excitation scheme sketched in Fig. 2(a), where an electron of charge  $-e < 0$  moves in the substrate at a constant velocity  $v > 0$  along a trajectory parallel to the slab interface at distance  $d$  (the nanoparticle is included in the next section).

The field generated by the electron [36] is (for  $\omega > 0$ )

$$\begin{aligned} \mathbf{E}_\omega^{(e)} &= \frac{E_{\omega 0}}{\varepsilon_1 \beta^2 \gamma} e^{i(\omega/v)x} \left[ -K_1 \left( \frac{\omega R}{v\gamma} \right) \mathbf{e}_R + \frac{i}{\gamma} K_0 \left( \frac{\omega R}{v\gamma} \right) \mathbf{e}_x \right], \\ \mathbf{H}_\omega^{(e)} &= \frac{E_{\omega 0}}{Z_0 \beta \gamma} e^{i(\omega/v)x} \left[ -K_1 \left( \frac{\omega R}{v\gamma} \right) \mathbf{e}_\Phi \right], \end{aligned} \quad (10)$$

where  $E_{\omega 0} = e Z_0 \omega / (4\pi^2 c)$  is a field amplitude,  $\beta = v/c$ ,  $\gamma = 1/\sqrt{1 - \varepsilon_1 \beta^2}$  is the Lorentz contraction factor,  $K_n$  are modified Bessel functions of the second kind, and  $(R, \Phi)$  are cylindrical coordinates coaxial with the charge trajectory, with coordinate unit vectors  $\mathbf{e}_R$  and  $\mathbf{e}_\Phi$ . The mirror symmetry of the electron field with respect to the reflection  $y \rightarrow -y$  is evident, and its deep subwavelength features are particularly marked in the sub-Cherenkov regime  $v < c/\sqrt{\varepsilon_1}$  we consider here, due to its radial exponential decay (see Appendix D).

In Fig. 2(b), we consider an electron beam of kinetic energy  $K = 395$  keV located at  $d = 10$  nm away from the 50-nm-thick slab in the setup considered above [Figs. 1(d) and 1(e)], and we plot the normalized modulus of the total field  $|\mathbf{E}_\omega|/E_{\omega 0}$  at the molecular resonance  $\lambda = 6.25$   $\mu\text{m}$ , together with its field dissymmetry factor

$$\Upsilon = \frac{|\mathbf{E}_\omega^{(A)}|}{|\mathbf{E}_\omega^{(S)}|}. \quad (11)$$

The electron-field decay length is of the order of 200 nm, and hence the chosen distance  $d$  enables this field to penetrate through the slab and to experience molecular chirality. This is explicitly demonstrated by the plot of  $\Upsilon$ , revealing a field asymmetry percentage of the order of 2% within the slab and, most importantly for our purposes, of the order of 1% in the substrate portion surrounding the electron beam. The nonvanishing of  $\Upsilon$  outside the slab signals markedly the occurrence of MOA. In Fig. 2(c), we consider the same situation as in Fig. 2(b) but with the inclusion of graphene and with the electron beam located at  $d = 30$  nm away from the slab. The total field profile now displays a modulation parallel to the slab of period  $172.8$  nm  $= 2\pi/k_p$  [see Fig. 1(e)] resulting from the interference of two excited graphene plasmon polaritons with parallel momenta  $k_y = k_p$  and  $k_y = -k_p$ . The impact of such counterpropagating plasmons on the MOA efficiency is displayed in the plot of  $\Upsilon$ , which dramatically reveals a modulation and an overall enhancement of the field asymmetry percentage [compare with Fig. 2(b)], a near-field interferometric phenomenon resulting from the interplay of plasmon excitation and field asymmetry. Indeed, the symmetry and antisymmetry in momentum space of  $\mathbf{E}_\omega^{(r)S}$  and  $\mathbf{E}_\omega^{(r)A}$  [see Eq. (8)], respectively, compel their leading plasmon contributions to have the  $y$  dependencies  $\mathbf{E}_\omega^{(r)S} \sim \cos(k_p y)$  and  $\mathbf{E}_\omega^{(r)A} \sim \sin(k_p y)$ , thus explaining the enhancement of  $\Upsilon$

close to those points where  $|\mathbf{E}_\omega^{(r)S}|$  and  $|\mathbf{E}_\omega^{(r)A}|$  are minimum and maximum, respectively, at once, due to their  $\pi/2$  dephasing (see Appendix D).

## V. CHIRAL SENSING BY CATHODOLUMINESCENCE

MOA is entirely due to molecular chirality, and consequently it can be harnessed to perform chiral sensing. In our fast-electron excitation scheme, this can be done by incorporating an off-axis nanoparticle located at  $y = h$  into the substrate just underneath the interface, as sketched in Fig. 2(a), and collecting in the superstrate its cathodoluminescence emission probability  $\Gamma(h)$ , the number of photons emitted per incoming electron per unit photon wavelength (see Appendix E). Since the reflected near field is spatially asymmetric (MOA), the emission probability  $\Gamma(-h)$  produced by the nanoparticle when placed in the mirror-symmetric position  $y = -h$  is different from  $\Gamma(h)$ , and hence chiral-sensing efficiency is provided here by the dissymmetry factor

$$\delta\Gamma(h) = 2 \frac{\Gamma(-h) - \Gamma(h)}{\Gamma(-h) + \Gamma(h)}. \quad (12)$$

In Fig. 3, we consider a graphene-free setup with an additional transparent conducting nanoparticle of radius  $a = 10$  nm, whose effective polarizability  $\alpha$  (in the nonretarded approximation) displays a plasmon resonance peak at  $\lambda = 5.8 \mu\text{m}$  [see Fig. 3(a)]. In Fig. 3(b), we set the nanoparticle position to  $h = 200$  nm and plot  $\Gamma$  and  $\delta\Gamma$  as functions of  $\lambda$  for different electron energies  $K$ . The emission spectrum  $\Gamma$  is characterized by the nanoparticle resonance peak at  $5.8 \mu\text{m}$  together with a slight dip due to molecular resonant absorption at  $6.25 \mu\text{m}$ , whereas  $\delta\Gamma$  displays only a peak at the molecular resonance, strong evidence of the

role played by the dissymmetry factor as an enantioselectivity quantifier. Note that higher electron energies reduce  $\Gamma$ , since the electron field in Eq. (10) decreases for large electron velocities. Conversely, the dissymmetry factor  $\delta\Gamma$  exhibits the opposite behavior, since higher electron velocities increase the  $S$  amplitude of the electron field at the expense of its  $P$  amplitude (see Appendix D), and this enhances the MOA (as discussed above). For comparison purposes, in the inset of Fig. 3(b) we plot the dimensionless circular-dichroism spectrum  $\text{Im}(\kappa)k_0L$ , which turns out to be about half of the dissymmetry factor  $\delta\Gamma$  at the lowest electron energy considered here and about 1 order of magnitude smaller at higher energies, thus showing that the chiral sensing technique we are discussing here is more efficient than standard circular dichroism. In Fig. 3(c), we set the electron energy to  $K = 395$  keV and plot  $\Gamma$  and  $\delta\Gamma$  as functions of the nanoparticle position  $h$  at different wavelengths close to the molecular resonance. The emission spectrum  $\Gamma$  fades for increasing values of  $h$  due to the radial exponential decay of the electron field, whereas the dissymmetry factor  $\delta\Gamma$  displays a maximum at  $h \simeq 150$  nm in agreement with the profile of the field dissymmetry factor  $\Upsilon$  in Fig. 2(b). On the other hand,  $\Gamma$  is poorly sensitive to  $\lambda$  over the chosen spectral bandwidth, whereas  $\delta\Gamma$  displays a marked dependence on  $\lambda$ , as further detailed in the inset of Fig. 3(c). As a comparison with other chiral-sensing techniques reported in the literature, we note that our approach does not require large-area micro-fabrication as in schemes exploiting plasmon-enhanced circular dichroism [12,13], where plasmonic inclusions are usually patterned on a surface [14,15]. In addition, our method exploits the whole spatial region of the chiral nanofilm where the field is not negligible, as opposed to the superchiral-fields technique, where the volume-averaged optical chirality is generally limited by its rapidly varying sign [10,22].

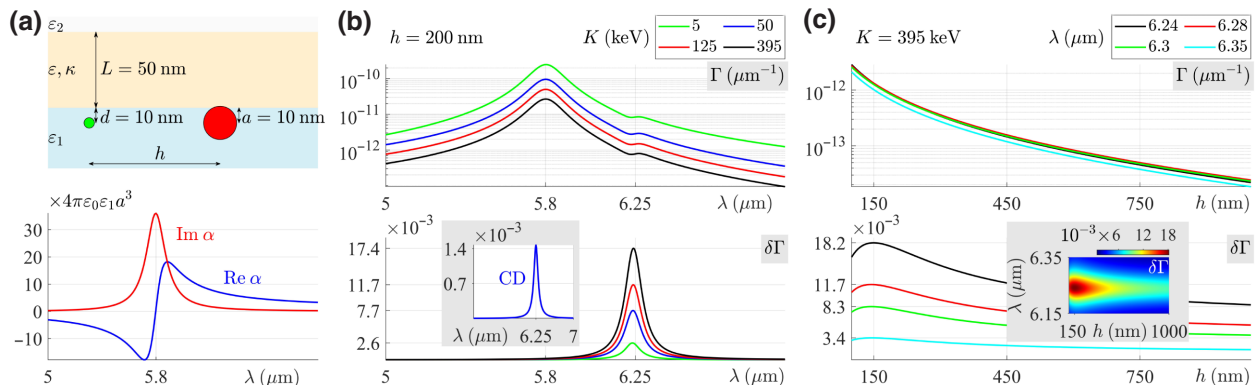


FIG. 3. Graphene-free chiral sensing. (a) Setup and nanoparticle effective polarizability  $\alpha$ . (b) Cathodoluminescence emission probability  $\Gamma$  and its dissymmetry factor  $\delta\Gamma$ , as functions of the wavelength, for a nanoparticle positioned at  $h = 200$  nm for various electron energies  $K$ . The dimensionless circular-dichroism (CD) spectrum  $\text{Im}(\kappa)k_0L$  of the slab is plotted in the inset for comparison purposes. (c) Dependence of  $\Gamma$  and  $\delta\Gamma$  on the nanoparticle position  $h$  for an electron energy  $K = 395$  keV at various wavelengths close to the molecular resonance. The detailed dependence of  $\delta\Gamma$  on  $h$  and  $\lambda$  is plotted in the inset.

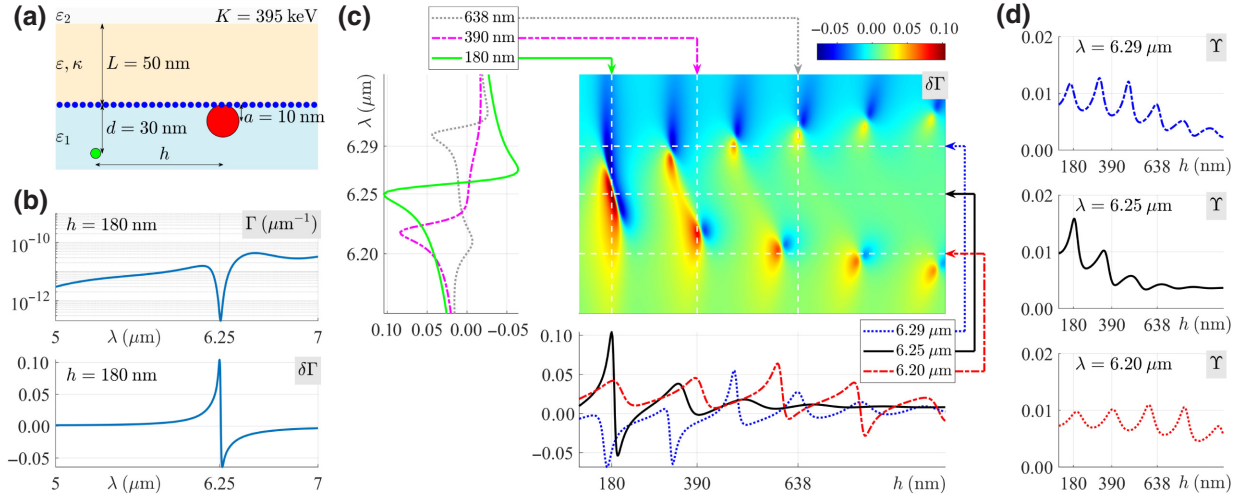


FIG. 4. Graphene-enhanced chiral sensing. (a) Chiral-sensing setup with inclusion of graphene and electron energy  $K = 395$  keV. (b) Cathodoluminescence emission probability  $\Gamma$  and its dissymmetry factor  $\delta\Gamma$ , as functions of the wavelength, for a nanoparticle positioned at  $h = 180$  nm. (c) Detailed dependence of  $\delta\Gamma$  on both the nanoparticle position (horizontal axis) and the wavelength (vertical axis). The bottom and side subplots display several slices of  $\delta\Gamma$  for selected wavelengths and nanoparticle positions, respectively. (d) Field dissymmetry factors  $\Upsilon(h)$  at the three wavelengths selected in the bottom plot of Fig. 4(c).

The setup with the inclusion of both graphene and a nanoparticle [see Fig. 4(a)] is even more interesting due to the interplay of MOA and the excitation of graphene plasmon polaritons. We hereafter set the electron energy to  $K = 395$  keV and, in Fig. 4(b), we report the wavelength dependence of  $\Gamma$  and  $\delta\Gamma$  for a nanoparticle positioned at  $h = 180$  nm. In this case the emission spectrum  $\Gamma$  does not exhibit a peak at  $\lambda = 5.8 \mu\text{m}$ , since the nanoparticle plasmon resonance is hybridized with the broadband graphene plasmon resonance [37,38], yielding an almost flat profile displaying only a pronounced dip at the molecular resonance at  $6.25 \mu\text{m}$ . The dissymmetry factor  $\delta\Gamma$  is very sensitive to molecular chirality, with a maximum value of about 0.1, which is 2 orders of magnitude larger than the dimensionless circular dichroism reported in the inset of Fig. 3(b), and its profile is not bell-shaped around the molecular resonance [as in Fig. 3(b)]. The further enhancement and spectral properties of  $\delta\Gamma$  are consequences of the complicated impact of the excitation of graphene plasmon polaritons on the MOA. To discuss such effects, in Fig. 4(c) we plot the detailed dependence of  $\delta\Gamma$  on both the nanoparticle position (horizontal axis) and the wavelength (vertical axis) and, in the bottom and side subplots, we report for the purpose of clarity several slices at selected wavelengths and nanoparticle positions. This plot should be compared with the inset of Fig. 3 (which is its counterpart for the graphene-free setup) just to realize the dramatic impact of the excitation of graphene plasmon polaritons on the enantioselectivity technique we are describing. The complicated pattern of  $\delta\Gamma$  displays a modulation with  $h$  whose period decreases for increasing wavelength, an unequivocal consequence of

the graphene plasmon-polariton dispersion  $k_p(\lambda)$ , which provides a marked wavelength dependence to the spatial interference pattern of the counterpropagating graphene plasmon polaritons. This can also be noticed in Fig. 4(d), where we plot the field dissymmetry factors  $\Upsilon(h)$  at the three wavelengths analyzed in the bottom plot of Fig. 4(c), their shapes qualitatively reproducing the slices of  $\delta\Gamma$ .

As a general observation about the experimental feasibility of MOA-based chiral sensing schemes, we remark that MOA is essentially a near-field phenomenon, and accordingly its detection requires nanophotonic techniques to scan the near-field profile. The relatively weak spatial asymmetry induced by MOA could hamper the practical usefulness of such techniques, since scanning-tip methods such as scanning near-field optical microscopy bring many experimental artifacts and challenges with them in their implementation, while far-field mapping of the radiation pattern of achiral emitters may lose some near-field information. However, in the scheme considered here, the point-dipole description of the nanoparticle is an excellent approximation (due to the size mismatch of the nanoparticle with the wavelength of light) and leads to relatively large values of the predicted dissymmetry factor  $\delta\Gamma$  close the molecular resonance, so that MOA detection should be experimentally accessible. Remarkably, in the context of chiral nanophotonics, methodologies have been proposed to capture the chiral near-field behavior by means of far-field measurements, and it is interesting that these schemes could possibly be generalized to support MOA detection. Examples of such methodologies are probing the polarization of radiation emitted by achiral fluorophores coated onto chiral nanostructures [39,40] and measuring

the chirality flux efficiency (chirality flux spectroscopy) [41,42].

As a final remark, we note that MOA detection schemes different from the one considered in this paper could generally make use of more structured nanocomposites, modeling of which cannot be done accurately with the dipolar description discussed here. However, generalizing the dipolar description to encompass multipolar effects is a relatively simple task [43], and, most importantly, this generalization does not conceptually hinder the detection of MOA, since each multipole is regarded as a pointlike entity and is thus fully sensitive to the near-field asymmetry.

## VI. DISCUSSION AND CONCLUSION

We show that the explicit symmetry breaking at the macroscopic scale provided by molecular chirality enables a geometrically symmetric chiral sample to respond in a spatially asymmetric fashion to a mirror-symmetric electromagnetic excitation. The field dissymmetry produced by the sample is particularly marked in the near field, thus suggesting avenues to perform efficient chiral sensing with the aid of nanophotonic strategies. We illustrate the concept by using a relativistic electron to trigger the asymmetric response of a chiral nanofilm, which is detected through the cathodoluminescence of an off-axis nanoparticle. The chiral sensitivity turns out to be 1 order of magnitude larger than the dimensionless circular dichroism, and its enhancement to 2 orders of magnitude due to the additional inclusion of graphene is solid evidence that focused tailoring of the nanophotonic platform could in principle lead to ultraefficient chiral sensing schemes. Therefore, the flexibility and potential of our findings stem from the number of nanoemitter sources available nowadays (semiconductor quantum dots, fluorescent molecules, etc.) and near-field optical probes (tapered optical fibers, aperture probes, solid metal tips, etc.).

Our chiral-sensing approach relies on the difference in the near field at two mirror-symmetric points produced by a single incident mirror-symmetric field, whereas standard techniques based on circular dichroism exploit the different absorption of two fields of opposite circular polarization. In addition to highlighting the operational difference between the two schemes, this comparison underlines the difference between their underpinning physical mechanisms, since in our case the absorption rates at two symmetric points are equal. Accordingly, in mirror optical activity, the asymmetry of the near field is sensitive to both the real and the imaginary parts of the chiral parameter  $\kappa$ .

Another advantage of our approach is that the setup for it does not require large-area microfabrication as in schemes exploiting plasmon-enhanced circular dichroism [12,13], where plasmonic inclusions are usually patterned on a surface [14,15] to increase the strength of the differential absorption signal. Remarkably, our technique exploits the

whole region of the homogeneous chiral nanofilm where the field is not negligible, conversely to what happens in plasmonic schemes relying on superchiral fields, where the volume-averaged optical chirality is generally limited by its rapidly varying sign over the volume [10,22].

## ACKNOWLEDGMENTS

The author acknowledges PRIN 2017 PELM (Grant No. 20177PSCKT) and useful discussions with Andrea Marini.

## APPENDIX A: HOMOGENEOUS CHIRAL MEDIA

The constitutive relations modeling (in the frequency domain) the electromagnetic response of a homogeneous and isotropic nonmagnetic chiral medium are

$$\begin{aligned}\mathbf{D}_\omega &= \varepsilon_0 \varepsilon \mathbf{E}_\omega - \frac{i}{c} \kappa \mathbf{H}_\omega, \\ \mathbf{B}_\omega &= \mu_0 \mathbf{H}_\omega + \frac{i}{c} \kappa \mathbf{E}_\omega,\end{aligned}\tag{A1}$$

where  $\varepsilon_0$  and  $\mu_0$  are the vacuum permittivity and permeability, respectively,  $c = 1/\sqrt{\varepsilon_0 \mu_0}$  is the speed of light,  $\varepsilon$  is the relative permittivity, and  $\kappa$  is the Pasteur parameter. The subscript  $\omega$  hereafter labels a quantity in the frequency domain according to the spectral analysis

$$f_\omega = \frac{1}{2\pi} \int_{-\infty}^{+\infty} dt e^{i\omega t} f(t).\tag{A2}$$

The parameter  $\kappa$  controls the coupling between the electric and magnetic responses of the medium and, therefore, the strength of its chirality. In the relevant case of a molecular medium where the chiral molecules are dispersed in a dielectric matrix medium, the permittivity and the chirality parameter can be modeled as

$$\begin{aligned}\varepsilon &= \varepsilon_b - \gamma_{\text{mol}} \left( \frac{1}{\hbar\omega - \hbar\omega_0 + i\Gamma} - \frac{1}{\hbar\omega + \hbar\omega_0 + i\Gamma} \right), \\ \kappa &= \beta_{\text{mol}} \left( \frac{1}{\hbar\omega - \hbar\omega_0 + i\Gamma} + \frac{1}{\hbar\omega + \hbar\omega_0 + i\Gamma} \right),\end{aligned}\tag{A3}$$

where  $\varepsilon_b$  is the background refractive index, and the coefficients  $\gamma_{\text{mol}}$  and  $\beta_{\text{mol}}$  are the amplitudes of the absorptive and chiral properties;  $\omega_0 = 2\pi c/\lambda_0$  corresponds to the wavelength  $\lambda_0$  of a molecular absorption resonance with a broadening determined by the damping  $\Gamma$ . Equations (A3) can be derived from the quantum equation of motion for the density matrix of a chiral molecule [44], whose lack of definite parity enables coupling between its electric and magnetic dipole moments, which in turn is responsible for the magnetoelectric coupling contained in Eq. (A1).

In the present paper, we focus on chiro-optical phenomena occurring in the infrared and choose alanine as



a specific molecular species for numerical calculations, since it exhibits marked vibrational circular dichroism [33, 34]. Accordingly, we hereafter set  $\varepsilon_b = 1.3$ ,  $\gamma_{\text{mol}} = 9.8 \times 10^{-4}$  eV,  $\beta_{\text{mol}} = 4.68 \times 10^{-5}$  eV,  $\hbar\omega_0 = 1.98 \times 10^{-1}$  eV (corresponding to the absorption resonance wavelength  $\lambda_0 = 6.25 \mu\text{m}$ ), and  $\Gamma = 1.6 \times 10^{-3}$  eV in order to emulate the resonant chiral response of an alanine enantiomer resulting from its vibrational mode at  $1600 \text{ cm}^{-1}$  (the two enantiomers have values of  $\beta_{\text{mol}}$ , and hence  $\kappa$ , with opposite signs).

## APPENDIX B: PARITY INDEFINITENESS OF THE ELECTROMAGNETIC FIELD IN CHIRAL MEDIA

An object is chiral if it is distinguishable from its mirror image, or, in other words, if its mirror image cannot be rigidly superposed on it use of rotations and translations only. Such a geometric definition is based on the mirror-reflection transformation, which consequently plays a pivotal role in the analysis of any physical effect produced by chirality. Since we focus on homogeneous isotropic chiral media in this paper, without loss of generality we consider the (active) reflection through the  $xz$  plane given by

$$\mathbf{r}' = (\mathbf{e}_x \mathbf{e}_x - \mathbf{e}_y \mathbf{e}_y + \mathbf{e}_z \mathbf{e}_z) \mathbf{r} \equiv \mathcal{R} \mathbf{r}, \quad (\text{B1})$$

where  $\mathbf{e}_x$ ,  $\mathbf{e}_y$ , and  $\mathbf{e}_z$  are the standard Cartesian unit vectors, and the dyadic notation  $(\mathbf{a}\mathbf{b})\mathbf{c} = (\mathbf{b} \cdot \mathbf{c}) \mathbf{a}$  is used. Basically, the dyadic  $\mathcal{R}$  changes the sign of the  $y$  component of the vector it operates on. While the mirror image of a geometric object  $O$  is the object  $O'$  whose points  $\mathbf{r}'$  are obtained from the points  $\mathbf{r}$  of  $O$  through  $\mathbf{r}' = \mathcal{R}\mathbf{r}$ , each physical entity has its own behavior under reflection. The most relevant behaviors are those of polar vectors  $\mathbf{P}(\mathbf{r})$ , axial vectors

$\mathbf{A}(\mathbf{r})$ , scalars  $s(\mathbf{r})$ , and pseudoscalars  $p(\mathbf{r})$ , whose mirror images are  $\mathbf{P}'(\mathbf{r}) = \mathcal{R}\mathbf{P}(\mathcal{R}\mathbf{r})$ ,  $\mathbf{A}'(\mathbf{r}) = -\mathcal{R}\mathbf{A}(\mathcal{R}\mathbf{r})$ ,  $s'(\mathbf{r}) = s(\mathcal{R}\mathbf{r})$ , and  $p'(\mathbf{r}) = -p(\mathcal{R}\mathbf{r})$ , respectively.

Reflection invariance (or mirror symmetry) is among the fundamental symmetries of nature, and states that if a complete experiment is subjected to mirror reflection, the resulting experiment should, in principle, be realizable (when the weak interaction can be neglected). The Maxwell equations  $\nabla \times \mathbf{E}_\omega = i\omega \mathbf{D}_\omega$  and  $\nabla \times \mathbf{H}_\omega = -i\omega \mathbf{D}_\omega$  evidently have mirror symmetry, since they are left invariant by the transformation  $\mathbf{r}' = \mathcal{R}\mathbf{r}$  combined with the requirement that  $\mathbf{E}_\omega$ ,  $\mathbf{D}_\omega$  are polar vectors and  $\mathbf{H}_\omega$ ,  $\mathbf{B}_\omega$  are axial vectors. (Mathematically, this is a consequence of the relation  $\nabla \times [\mathcal{R}\mathbf{F}(\mathcal{R}\mathbf{r})] = -\mathcal{R}[(\nabla \times \mathbf{F})(\mathcal{R}\mathbf{r})]$  holding for any vector field  $\mathbf{F}(\mathbf{r})$ .) Enforcing these properties on the constitutive relations in Eq. (A1), it is straightforward to prove that, under reflection,  $\varepsilon' = \varepsilon$  and  $\kappa' = -\kappa$ , i.e., the permittivity  $\varepsilon$  is a scalar and the chiral parameter  $\kappa$  is a pseudoscalar. Since opposite molecular enantiomers provide opposite chiral parameters, it follows that the mirror image of a chiral medium is precisely its opposite enantiomeric medium, as expected. As a consequence, reflection invariance can be rephrased as follows here: the mirror image of the electromagnetic field existing in a chiral medium is a physically realizable electromagnetic field inside the opposite enantiomeric medium. This well-known fact is the starting point of the following analysis, and hence it is convenient to summarize it mathematically by stating that if the fields  $\mathbf{E}_\omega$ ,  $\mathbf{H}_\omega$  satisfy the Maxwell equations with chiral parameter  $\kappa$ , the mirror images  $\mathbf{E}'_\omega$ ,  $\mathbf{H}'_\omega$  satisfy the Maxwell equations with chiral parameter  $-\kappa$ , and vice versa, i.e.,

$$\begin{cases} \nabla \times \mathbf{E}_\omega = i\omega \left( \mu_0 \mathbf{H}_\omega + \frac{i}{c} \kappa \mathbf{E}_\omega \right) \\ \nabla \times \mathbf{H}_\omega = i\omega \left( -\varepsilon_0 \varepsilon \mathbf{E}_\omega + \frac{i}{c} \kappa \mathbf{H}_\omega \right) \end{cases} \Leftrightarrow \begin{cases} \nabla \times \mathbf{E}'_\omega = i\omega \left( \mu_0 \mathbf{H}'_\omega - \frac{i}{c} \kappa \mathbf{E}'_\omega \right) \\ \nabla \times \mathbf{H}'_\omega = i\omega \left( -\varepsilon_0 \varepsilon \mathbf{E}'_\omega - \frac{i}{c} \kappa \mathbf{H}'_\omega \right) \end{cases}. \quad (\text{B2})$$

$$\begin{aligned} \mathbf{E}'_\omega(\mathbf{r}) &= \mathcal{R}\mathbf{E}_\omega(\mathcal{R}\mathbf{r}) \\ \mathbf{H}'_\omega(\mathbf{r}) &= -\mathcal{R}\mathbf{H}_\omega(\mathcal{R}\mathbf{r}) \end{aligned}$$

As with any fundamental symmetry, reflection invariance of physical laws holds only for a ‘‘complete experiment,’’ i.e., for an isolated system. In our case the isolated system is composed of an electromagnetic field and a chiral medium, whose global mirror reflection leaves the Maxwell equations invariant. What is remarkable here is that reflection invariance also provides a spatial dissymmetry property of the single electromagnetic field existing in a chiral medium. In order to discuss this point, it is

convenient to consider the concept of a MSF, that is, an electromagnetic field such that  $\mathbf{E}_\omega$ ,  $\mathbf{H}_\omega$  are identical to their mirror images  $\mathbf{E}_\omega = \mathbf{E}'_\omega$ ,  $\mathbf{H}_\omega = \mathbf{H}'_\omega$  or, equivalently, satisfy the relations

$$\begin{aligned} \mathbf{E}_\omega(\mathbf{r}) &= \mathcal{R}\mathbf{E}_\omega(\mathcal{R}\mathbf{r}), \\ \mathbf{H}_\omega(\mathbf{r}) &= -\mathcal{R}\mathbf{H}_\omega(\mathcal{R}\mathbf{r}). \end{aligned} \quad (\text{B3})$$

Now an electromagnetic field in a chiral medium is such that  $\mathbf{E}_\omega, \mathbf{H}_\omega$  satisfy the left system of Eq. (B2) and hence, by reflection invariance, their mirror images  $\mathbf{E}'_\omega, \mathbf{H}'_\omega$  satisfy the right system, which is different from the left one due to the sign reversal of  $\kappa$ . Consequently, the relations  $\mathbf{E}_\omega = \mathbf{E}'_\omega, \mathbf{H}_\omega = \mathbf{H}'_\omega$  are forbidden by chirality, and this proves that MSFs do not exist in chiral media. In other words, in a homogeneous and isotropic chiral medium, the microscopic lack of mirror symmetry of chiral molecules is responsible for a macroscopic spatial dissymmetry of the electromagnetic field. The peculiarity of such spatial dissymmetry becomes even more evident when we note that, conversely, MSFs are allowed in achiral media. As a matter of fact, by repeating the above reasoning in the case  $\kappa = 0$ , it is evident that the mirror images  $\mathbf{E}'_\omega, \mathbf{H}'_\omega$  satisfy the same equations as  $\mathbf{E}_\omega, \mathbf{H}_\omega$  so that MSFs in achiral media are not ruled out. As an example, the electromagnetic field produced by an electric dipole  $\mathbf{p}_\omega$  in an achiral medium is easily seen to be a MSF (with respect to the reflection  $\mathcal{R}$ ) if the dipole moment lies in the  $xz$  plane (i.e., if  $\mathbf{e}_y \cdot \mathbf{p}_\omega = 0$ ).

The mirror dissymmetry of the electromagnetic field in chiral media can also be analyzed in a different way, which sheds further light upon such a fundamental trait. After solving for the magnetic fields  $\mathbf{H}_\omega = (1/i\omega\mu_0)(\nabla \times \mathbf{E}_\omega + k_0\kappa\mathbf{E}_\omega)$  and  $\mathbf{H}'_\omega = (1/i\omega\mu_0)(\nabla \times \mathbf{E}'_\omega - k_0\kappa\mathbf{E}'_\omega)$  from the curl equations for  $\mathbf{E}_\omega$  and  $\mathbf{E}'_\omega$  in Eq. (B2), the curl equations for  $\mathbf{H}_\omega$  and  $\mathbf{H}'_\omega$  yield

$$\begin{aligned} [k_0^2(\varepsilon - \kappa^2) - \nabla \times \nabla \times] \mathbf{E}_\omega - 2k_0\kappa \nabla \times \mathbf{E}_\omega &= 0, \\ [k_0^2(\varepsilon - \kappa^2) - \nabla \times \nabla \times] \mathbf{E}'_\omega + 2k_0\kappa \nabla \times \mathbf{E}'_\omega &= 0, \end{aligned} \quad (\text{B4})$$

where  $k_0 = \omega/c$  is the vacuum wave number. Consider now the electric field decomposition  $\mathbf{E}_\omega = \mathbf{E}_\omega^S + \mathbf{E}_\omega^A$ , where the fields

$$\begin{aligned} \mathbf{E}_\omega^S &= \frac{1}{2}(\mathbf{E}_\omega + \mathbf{E}'_\omega), \\ \mathbf{E}_\omega^A &= \frac{1}{2}(\mathbf{E}_\omega - \mathbf{E}'_\omega) \end{aligned} \quad (\text{B5})$$

have definite parity, since  $\mathbf{E}_\omega^S$  is even (the symmetric part) and  $\mathbf{E}_\omega^A$  is odd (the antisymmetric part) under reflection. By definition, a MSF is such that  $\mathbf{E}_\omega = \mathbf{E}_\omega^S$  (i.e.,  $\mathbf{E}_\omega^A = 0$ ), whereas a MAF is characterized by the condition  $\mathbf{E}_\omega = \mathbf{E}_\omega^A$  (i.e.,  $\mathbf{E}_\omega^S = 0$ ). From Eq. (B4), it is straightforward to obtain the equations

$$\begin{aligned} [k_0^2(\varepsilon - \kappa^2) - \nabla \times \nabla \times] \mathbf{E}_\omega^S &= 2k_0\kappa \nabla \times \mathbf{E}_\omega^A, \\ [k_0^2(\varepsilon - \kappa^2) - \nabla \times \nabla \times] \mathbf{E}_\omega^A &= 2k_0\kappa \nabla \times \mathbf{E}_\omega^S, \end{aligned} \quad (\text{B6})$$

showing that the medium chirality  $\kappa$  physically couples the symmetric and the antisymmetric parts of the electric

field. The structure of such a coupling clearly reveals that  $\mathbf{E}_\omega^S$  and  $\mathbf{E}_\omega^A$  cannot separately vanish, or, in other words, that the chiral medium hosts neither MSFs (as just proven above) nor MAFs. We conclude that the field always has symmetric and antisymmetric parts and therefore is an IPF. Note that in achiral media, Eq. (B6) with  $\kappa = 0$  shows that the symmetric and the antisymmetric parts are not coupled, and hence both MSFs and MAFs are separately allowed, so that electromagnetic parity indefiniteness does not occur.

### APPENDIX C: MIRROR OPTICAL ACTIVITY

As discussed in the above appendix, the electromagnetic field in a chiral medium necessarily has indefinite parity (it is an IPF), whereas in an achiral medium the field can have definite parity (it can be a MSF or MAF). It is therefore interesting to investigate the effect of a MSF impinging onto a chiral slab, since an IPF is expected to show up in the surrounding achiral environment as a consequence of the IPF excited inside the bulk of the chiral slab. Most remarkably, the dissymmetry of the reflected (and transmitted) field is a genuinely chiro-optical effect, namely MOA, since it is entirely due to the slab chirality, and its detection effectively amounts to a measurement of the chiral parameter  $\kappa$ .

#### 1. Interaction of a chiral slab with an electromagnetic field

As a prelude to the discussion of MOA, it is essential to revise the full response of a chiral slab to an impinging electromagnetic field. With reference to Fig. 5, we consider a chiral homogeneous isotropic medium of permittivity  $\varepsilon$  and chiral parameter  $\kappa$  (see Appendix A) filling the slab  $0 < z < L$ , surrounded by a substrate in  $z < 0$  and a superstrate in  $z > L$  of permittivities  $\varepsilon_1$  and  $\varepsilon_2$ ,

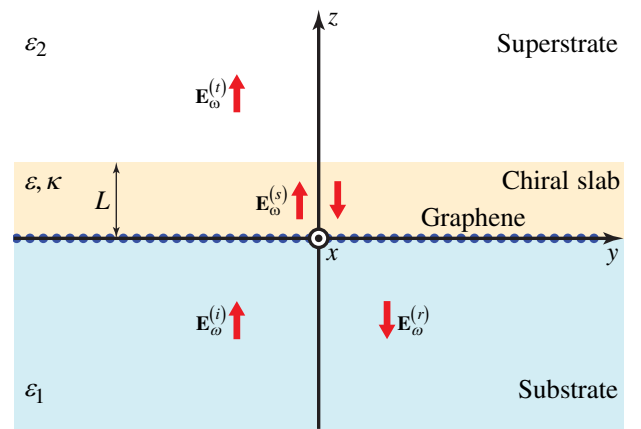


FIG. 5. Geometry of a chiral slab surrounded by an achiral environment made up of a substrate, a graphene sheet, and a dielectric. Red arrows sketch the field configuration.

respectively. In order to consider a slightly more general situation, we also incorporate a graphene sheet lying in the  $z = 0$  plane between the substrate and the chiral slab. Even though graphene is not essential for the onset of MOA, it is nonetheless remarkable that the excitation of plasmon polaritons combined with field dissymmetry triggers a near-field interferometric mechanism able to enhance enantiomeric sensing (see below).

Because of the planar geometry of the setup, we make use of the angular-spectrum-representation technique, and the incident field  $\mathbf{E}_\omega^{(i)}$  in  $z < 0$  is

$$\mathbf{E}_\omega^{(i)} = \int d^2\mathbf{k}_\parallel e^{i\mathbf{k}_\parallel \cdot \mathbf{r}_\parallel} e^{ik_{1z}z} \left[ U_S^{(i)} \mathbf{u}_S + U_P^{(i)} \left( \mathbf{u}_P - \frac{k_\parallel}{k_{1z}} \mathbf{e}_z \right) \right], \quad (\text{C1})$$

where  $\mathbf{r}_\parallel = x\mathbf{e}_x + y\mathbf{e}_y$ ,  $\mathbf{k}_\parallel = k_x\mathbf{e}_x + k_y\mathbf{e}_y$  is the parallel wave number,  $k_{1z} = \sqrt{k_0^2\epsilon_1 - k_\parallel^2}$  ( $\text{Im } k_{1z} > 0$ ),  $\mathbf{u}_S(\mathbf{k}_\parallel) = \mathbf{e}_z \times (\mathbf{k}_\parallel/k_\parallel)$  and  $\mathbf{u}_P(\mathbf{k}_\parallel) = (\mathbf{k}_\parallel/k_\parallel)$  are the transverse electric ( $S$ ) and transverse magnetic ( $P$ ) unit vectors, and  $U_S^{(i)}(\mathbf{k}_\parallel)$  and  $U_P^{(i)}(\mathbf{k}_\parallel)$  are the  $S$  and  $P$  spectral amplitudes of the incident ( $i$ ) field. The unit vectors  $\mathbf{u}_S, \mathbf{u}_P$  are an orthonormal basis of the parallel plane of vectors  $\mathbf{A}_\parallel = A_x\mathbf{e}_x + A_y\mathbf{e}_y$ . The ordered triple  $(\mathbf{u}_P, \mathbf{u}_S, \mathbf{e}_z)$  is a left-handed orthonormal basis, since  $\mathbf{u}_P \times \mathbf{u}_S = \mathbf{e}_z$ ,  $\mathbf{e}_z \times \mathbf{u}_P = \mathbf{u}_S$ , and  $\mathbf{u}_S \times \mathbf{e}_z = \mathbf{u}_P$ . The  $j = \{S, P\}$  component of the incident field is given by

$$U_j^{(i)}(\mathbf{k}_\parallel) = \mathbf{u}_j(\mathbf{k}_\parallel) \cdot \int \frac{d^2\mathbf{r}_\parallel}{(2\pi)^2} e^{-i\mathbf{k}_\parallel \cdot \mathbf{r}_\parallel} \mathbf{E}_\omega^{(i)}(\mathbf{r}_\parallel + 0^- \mathbf{e}_z). \quad (\text{C2})$$

The reflected field  $\mathbf{E}_\omega^{(r)}$  in  $z < 0$  and the transmitted field  $\mathbf{E}_\omega^{(t)}$  in  $z > L$  are

$$\begin{aligned} \mathbf{E}_\omega^{(r)} &= \int d^2\mathbf{k}_\parallel e^{i\mathbf{k}_\parallel \cdot \mathbf{r}_\parallel} e^{-ik_{1z}z} \\ &\quad \times \left[ U_S^{(r)} \mathbf{u}_S + U_P^{(r)} \left( \mathbf{u}_P + \frac{k_\parallel}{k_{1z}} \mathbf{e}_z \right) \right], \\ \mathbf{E}_\omega^{(t)} &= \int d^2\mathbf{k}_\parallel e^{i\mathbf{k}_\parallel \cdot \mathbf{r}_\parallel} e^{ik_{2z}(z-L)} \\ &\quad \times \left[ U_S^{(t)} \mathbf{u}_S + U_P^{(t)} \left( \mathbf{u}_P - \frac{k_\parallel}{k_{2z}} \mathbf{e}_z \right) \right], \end{aligned} \quad (\text{C3})$$

where  $k_{2z} = \sqrt{k_0^2\epsilon_2 - k_\parallel^2}$  ( $\text{Im } k_{2z} > 0$ ) and  $U_S^{(r)}(\mathbf{k}_\parallel)$ ,  $U_P^{(r)}(\mathbf{k}_\parallel)$ ,  $U_S^{(t)}(\mathbf{k}_\parallel)$ ,  $U_P^{(t)}(\mathbf{k}_\parallel)$  are the  $S$  and  $P$  spectral amplitudes of the reflected ( $r$ ) and transmitted ( $t$ ) fields. The field  $\mathbf{E}_\omega^{(s)}$  in  $0 < z < L$  is the most general solution of the

first equation of Eq. (B4), given by

$$\begin{aligned} \mathbf{E}_\omega^{(s)} &= \int d^2\mathbf{k}_\parallel e^{i\mathbf{k}_\parallel \cdot \mathbf{r}_\parallel} \sum_{\sigma\tau} e^{i\sigma K_{z\tau}z} \\ &\quad \times \left[ n \frac{k_0}{i\sigma K_{z\tau}} \left( \frac{\kappa^2}{\sqrt{\epsilon\kappa^2}} + \tau \right) \mathbf{u}_S + \left( \mathbf{u}_P - \frac{k_\parallel}{\sigma K_{z\tau}} \mathbf{e}_z \right) \right] U_\tau^{(\sigma)}, \end{aligned} \quad (\text{C4})$$

where  $n = \sqrt{\epsilon\kappa^2}/\kappa$ , and it is a superposition of circularly polarized plane waves whose spectral amplitudes are  $U_\tau^{(\sigma)}(\mathbf{k}_\parallel)$ . These waves are labeled by the parallel wave number  $\mathbf{k}_\parallel$ , the sign  $\sigma = \pm 1$  of the transverse wave number  $K_{z\tau} = \sqrt{k_0^2(n + \tau\kappa)^2 - k_\parallel^2}$  ( $\text{Im } K_{z\tau} > 0$ ), and the circular-polarization sense  $\tau = \pm 1$ . Indeed, the wave vector  $\mathbf{K}_\tau^{(\sigma)} = \mathbf{k}_\parallel + \sigma K_{z\tau} \mathbf{e}_z$  and the polarization  $\mathbf{V}_\tau^{(\sigma)} = n(k_0/i\sigma K_{z\tau}) \left( (\kappa^2/\sqrt{\epsilon\kappa^2}) + \tau \right) \mathbf{u}_S + [\mathbf{u}_P - (k_\parallel/\sigma K_{z\tau}) \mathbf{e}_z]$  of the basic plane waves are easily seen to satisfy the relation

$$\mathbf{K}_\tau^{(\sigma)} \times \mathbf{V}_\tau^{(\sigma)} = i\tau k_0 (n + \tau\kappa) \mathbf{V}_\tau^{(\sigma)}, \quad (\text{C5})$$

showing their transversality ( $\mathbf{K}_\tau^{(\sigma)} \cdot \mathbf{V}_\tau^{(\sigma)} = 0$ ) and circular polarization ( $\mathbf{V}_\tau^{(\sigma)} \cdot \mathbf{V}_\tau^{(\sigma)} = 0$ ) with sense  $\tau$ . The state of circular polarization imposes a severe constraint between the  $S$  and  $P$  components of the field in Eq. (C4). Such an  $S$ - $P$  coupling is produced entirely by chirality, and it is particularly strong in the evanescent part of the spectrum. Indeed, for  $k_\parallel \gg k_0$ , the  $S$  component of  $\mathbf{V}_\tau^{(\sigma)}$  fades because  $K_{z\tau} \simeq ik_\parallel$  in its denominator, whereas the  $P$  component approaches its limit  $\mathbf{u}_P + i\sigma \mathbf{e}_z$  (which is the same circular polarization state as the one accounting for the transverse spin of evanescent waves in achiral media [35]). The fact that the evanescent part of the spectrum is almost entirely  $P$  is physically clear, since the isotropy of the chiral medium together with the field transversality [ $\nabla \cdot \mathbf{E}_\omega^{(s)} = 0$ ; see the first equation of Eq. (B4)] implies that the  $P$ - $z$  part is asymptotically circularly polarized, and this forces the asymptotic vanishing behavior of the orthogonal  $S$  component to preserve the circular polarization state of the overall plane wave.

Graphene is modeled through a surface current density flowing in the plane  $z = 0$  given by  $\mathbf{K}_{\omega\parallel} = \sigma_G(\omega) \mathbf{E}_{\omega\parallel}$ , where  $\sigma_G(\omega)$  is the surface conductivity of the graphene (see Appendix F) and  $\mathbf{E}_{\omega\parallel} = E_{\omega x} \mathbf{e}_x + E_{\omega y} \mathbf{e}_y$  is the in-plane part of the total electric field at  $z = 0$ . By enforcing the boundary conditions at  $z = 0$  and  $z = L$

$$\begin{aligned}
& \left\{ \begin{aligned} \mathbf{E}_{\omega\parallel}(\mathbf{r}_{\parallel}+0^-\mathbf{e}_z) - \mathbf{E}_{\omega\parallel}(\mathbf{r}_{\parallel}+0^+\mathbf{e}_z) &= 0 \\ \left[ \mathbf{H}_{\omega}(\mathbf{r}_{\parallel}+0^-\mathbf{e}_z) - \mathbf{H}_{\omega}(\mathbf{r}_{\parallel}+0^+\mathbf{e}_z) \right] \times \mathbf{e}_z &= \sigma_G \mathbf{E}_{\omega\parallel}(\mathbf{r}_{\parallel}+0\mathbf{e}_z) \end{aligned} \right. \\
& \left\{ \begin{aligned} \mathbf{E}_{\omega\parallel}(\mathbf{r}_{\parallel}+L^-\mathbf{e}_z) - \mathbf{E}_{\omega\parallel}(\mathbf{r}_{\parallel}+L^+\mathbf{e}_z) &= \mathbf{0} \\ \left[ \mathbf{H}_{\omega}(\mathbf{r}_{\parallel}+L^-\mathbf{e}_z) - \mathbf{H}_{\omega}(\mathbf{r}_{\parallel}+L^+\mathbf{e}_z) \right] \times \mathbf{e}_z &= \mathbf{0} \end{aligned} \right. \end{aligned} \quad (C6)$$

we obtain

$$\begin{aligned}
& \left\{ \begin{aligned} \sum_{\sigma\tau} \left( \frac{k_0}{2ik_{1z}} \right) \left[ \varepsilon + \frac{\varepsilon + \tau\sqrt{\varepsilon\kappa^2}}{\sigma K_{z\tau}} (k_{1z} + k_0 Z_0 \sigma_G) \right] \tau U_{\tau}^{(\sigma)} &= n U_S^{(i)} \\ \sum_{\sigma\tau} e^{i\sigma K_{z\tau} L} \left( \varepsilon - \frac{\varepsilon + \tau\sqrt{\varepsilon\kappa^2}}{\sigma K_{z\tau}} k_{2z} \right) \tau U_{\tau}^{(\sigma)} &= 0 \\ \sum_{\sigma\tau} \left( \frac{k_{1z}}{2\varepsilon_1} \right) \left( \frac{\varepsilon + \tau\sqrt{\varepsilon\kappa^2}}{\sigma K_{z\tau}} + \frac{\varepsilon_1}{k_{1z}} + \frac{Z_0 \sigma_G}{k_0} \right) U_{\tau}^{(\sigma)} &= U_P^{(i)} \\ \sum_{\sigma\tau} e^{i\sigma K_{z\tau} L} \left( \varepsilon_2 - \frac{\varepsilon + \tau\sqrt{\varepsilon\kappa^2}}{\sigma K_{z\tau}} k_{2z} \right) U_{\tau}^{(\sigma)} &= 0 \end{aligned} \right. \quad , \\
& \left\{ \begin{aligned} U_S^{(r)} &= -U_S^{(i)} + n \sum_{\sigma\tau} \left[ \frac{k_0}{i\sigma K_{z\tau}} \left( \frac{\kappa^2}{\sqrt{\varepsilon\kappa^2}} + \tau \right) \right] U_{\tau}^{(\sigma)} \\ U_P^{(r)} &= -U_P^{(i)} + \sum_{\sigma\tau} U_{\tau}^{(\sigma)} \\ U_S^{(t)} &= n \sum_{\sigma\tau} e^{i\sigma K_{z\tau} L} \left[ \frac{k_0}{i\sigma K_{z\tau}} \left( \frac{\kappa^2}{\sqrt{\varepsilon\kappa^2}} + \tau \right) \right] U_{\tau}^{(\sigma)} \\ U_P^{(t)} &= \sum_{\sigma\tau} e^{i\sigma K_{z\tau} L} U_{\tau}^{(\sigma)} \end{aligned} \right. \quad , \end{aligned} \quad (C7)$$

where  $Z_0 = \sqrt{\mu_0/\varepsilon_0}$  is the vacuum impedance. In matrix notation, Eq. (C7) can be cast as

$$\begin{aligned}
\underline{\underline{M}} \underline{U} &= n U_S^{(i)} \underline{V}_S + U_P^{(i)} \underline{V}_P, \\
\left\{ \begin{aligned} U_S^{(r)} &= -U_S^{(i)} + n \underline{W}_S^{(r)} \cdot \underline{U} \\ U_P^{(r)} &= -U_P^{(i)} + \underline{W}_P^{(r)} \cdot \underline{U} \\ U_S^{(t)} &= n \underline{W}_S^{(t)} \cdot \underline{U} \\ U_P^{(t)} &= \underline{W}_P^{(t)} \cdot \underline{U} \end{aligned} \right. \quad , \end{aligned} \quad (C8)$$

where  $\underline{\underline{M}}$  is the system matrix,  $\underline{U} = (U_+^{(+)} \quad U_-^{(+)} \quad U_+^{(-)} \quad U_-^{(-)})^T$ ,  $\underline{V}_S = (1 \quad 0 \quad 0 \quad 0)^T$ ,  $\underline{V}_P = (0 \quad 0 \quad 1 \quad 0)^T$ , and the vectors  $\underline{W}_S^{(r)}$ ,  $\underline{W}_P^{(r)}$ ,  $\underline{W}_S^{(t)}$ ,  $\underline{W}_P^{(t)}$  are easily read from the second system in Eq. (C7). Substituting the formal solution  $\underline{U} = \underline{\underline{M}}^{-1} (n U_S^{(i)} \underline{V}_S + U_P^{(i)} \underline{V}_P)$  of the first system of Eq. (C8) into the second system, we obtain

$$\begin{aligned}
& \left\{ \begin{aligned} \begin{pmatrix} U_S^{(r)} \\ U_P^{(r)} \end{pmatrix} &= \begin{pmatrix} R_{SS} & nR_{SP} \\ nR_{PS} & R_{PP} \end{pmatrix} \begin{pmatrix} U_S^{(i)} \\ U_P^{(i)} \end{pmatrix} \\ \begin{pmatrix} U_S^{(t)} \\ U_P^{(t)} \end{pmatrix} &= \begin{pmatrix} T_{SS} & nT_{SP} \\ nT_{PS} & T_{PP} \end{pmatrix} \begin{pmatrix} U_S^{(i)} \\ U_P^{(i)} \end{pmatrix} \end{aligned} \right. \quad , \\
& \left\{ \begin{aligned} \begin{pmatrix} R_{SS} & R_{SP} \\ R_{PS} & R_{PP} \end{pmatrix} &= \begin{pmatrix} -1 + n^2 \underline{W}_S^{(r)} \cdot \underline{\underline{M}}^{-1} \underline{V}_S & \underline{W}_S^{(r)} \cdot \underline{\underline{M}}^{-1} \underline{V}_P \\ \underline{W}_P^{(r)} \cdot \underline{\underline{M}}^{-1} \underline{V}_S & -1 + \underline{W}_P^{(r)} \cdot \underline{\underline{M}}^{-1} \underline{V}_P \end{pmatrix} \\ \begin{pmatrix} T_{SS} & T_{SP} \\ T_{PS} & T_{PP} \end{pmatrix} &= \begin{pmatrix} n^2 \underline{W}_S^{(t)} \cdot \underline{\underline{M}}^{-1} \underline{V}_S & \underline{W}_S^{(t)} \cdot \underline{\underline{M}}^{-1} \underline{V}_P \\ \underline{W}_P^{(t)} \cdot \underline{\underline{M}}^{-1} \underline{V}_S & \underline{W}_P^{(t)} \cdot \underline{\underline{M}}^{-1} \underline{V}_P \end{pmatrix} \end{aligned} \right. \quad , \end{aligned} \quad (C9)$$

which directly provide the reflected and transmitted amplitudes in terms of the incident ones.



Inserting these amplitudes into Eq. (C3), we eventually obtain

$$\begin{aligned}\mathbf{E}_\omega^{(r)} &= \int d^2\mathbf{k}_\parallel e^{i\mathbf{k}_\parallel \cdot \mathbf{r}_\parallel} e^{-ik_{1z}z} \left[ \left( R_{SS}U_S^{(i)} + nR_{SP}U_P^{(i)} \right) \mathbf{u}_S + \left( nR_{PS}U_S^{(i)} + R_{PP}U_P^{(i)} \right) \left( \mathbf{u}_P + \frac{k_\parallel}{k_{1z}} \mathbf{e}_z \right) \right], \\ \mathbf{E}_\omega^{(t)} &= \int d^2\mathbf{k}_\parallel e^{i\mathbf{k}_\parallel \cdot \mathbf{r}_\parallel} e^{ik_{2z}(z-L)} \left[ \left( T_{SS}U_S^{(i)} + nT_{SP}U_P^{(i)} \right) \mathbf{u}_S + \left( nT_{PS}U_S^{(i)} + T_{PP}U_P^{(i)} \right) \left( \mathbf{u}_P - \frac{k_\parallel}{k_{2z}} \mathbf{e}_z \right) \right].\end{aligned}\quad (\text{C10})$$

which yield the reflected and transmitted fields in terms of the amplitudes of the incident field and hence provide the full electromagnetic response of the chiral slab. Note that each of the  $S$  and  $P$  components of the reflected and transmitted field depends on both  $U_S^{(i)}$  and  $U_P^{(i)}$  as a consequence of the  $S$ - $P$  coupling produced by the slab chirality. Since in achiral media the  $S$  and  $P$  components are uncoupled, the mixing coefficients  $R_{SP}$ ,  $R_{PS}$ ,  $T_{SP}$ ,  $T_{PS}$  are entirely due to chirality and are essential in the theoretical discussion of MOA (see below). It is worth noting that the reflection and transmission matrices  $R$  and  $T$  in Eq. (C9) are left invariant by the reflection  $\mathbf{k}_\parallel \rightarrow \mathcal{R}\mathbf{k}_\parallel$  and by the chirality reversal  $\kappa \rightarrow -\kappa$  since  $n^2 = \varepsilon$  and, from Eq. (C7), the matrix  $\underline{M}$  and the vectors  $\underline{W}$  depend only on  $k_\parallel = \sqrt{k_x^2 + k_y^2}$  and  $\kappa^2$ .

In Fig. 6(a), we plot the reflection coefficients as functions of the normalized parallel wave vector  $k_\parallel/k_0$  and the wavelength  $\lambda = 2\pi c/\omega$ , characterizing a chiral slab of thickness  $L = 0.05 \mu\text{m}$  filled with the molecular medium discussed in Appendix A, surrounded by a substrate of permittivity  $\varepsilon_1 = 1.2$  and by vacuum as a superstrate of permittivity  $\varepsilon_2 = 1$  (without a graphene sheet). The molecular resonance peak at  $\lambda = 6.25 \mu\text{m}$  is evident together

with its peculiar impact on  $R_{PS}$  and  $R_{PP}$  in the evanescent part of the spectrum. This is due to the dominant  $P$  character of the spectrum of the slab field for  $k_\parallel \gg k_0$  (as discussed above), and, accordingly, the reflected-field spectrum is asymptotically almost  $P$ . Remarkably, the fundamental mixing coefficient  $R_{PS}$  increases with  $k_\parallel$ . This is a consequence of the fact that the mixing reflection process where a photon of kind  $S$  is reflected into a photon of kind  $P$  is extremely sensitive to the incident magnetic field

$$\begin{aligned}\mathbf{H}_\omega^{(i)} &= \frac{1}{i\omega\mu_0} \nabla \times \mathbf{E}_\omega^{(i)} = \frac{1}{Z_0} \int d^2\mathbf{k}_\parallel e^{i\mathbf{k}_\parallel \cdot \mathbf{r}_\parallel} e^{ik_{1z}z} \\ &\times \left[ \frac{k_0}{k_{1z}} \varepsilon_1 U_P^{(i)} \mathbf{u}_S - \frac{k_{1z}}{k_0} U_S^{(i)} \left( \mathbf{u}_P - \frac{k_\parallel}{k_{1z}} \mathbf{e}_z \right) \right],\end{aligned}\quad (\text{C11})$$

and the longitudinal wave number  $k_{1z}$  multiplying  $U_S^{(i)}$  is responsible for the boosting of  $R_{PS}$  for  $k_\parallel \gg k_0$ . In Fig. 6(b), we plot the coefficients for the same setup encompassing a graphene sheet of Fermi energy  $E_F = 0.5 \text{ eV}$ , and the occurrence of the graphene plasmon resonance is manifest along the stripe  $30k_0 < k_\parallel < 40k_0$  (except for the purely  $S$  coefficient  $R_{SS}$ , as expected).

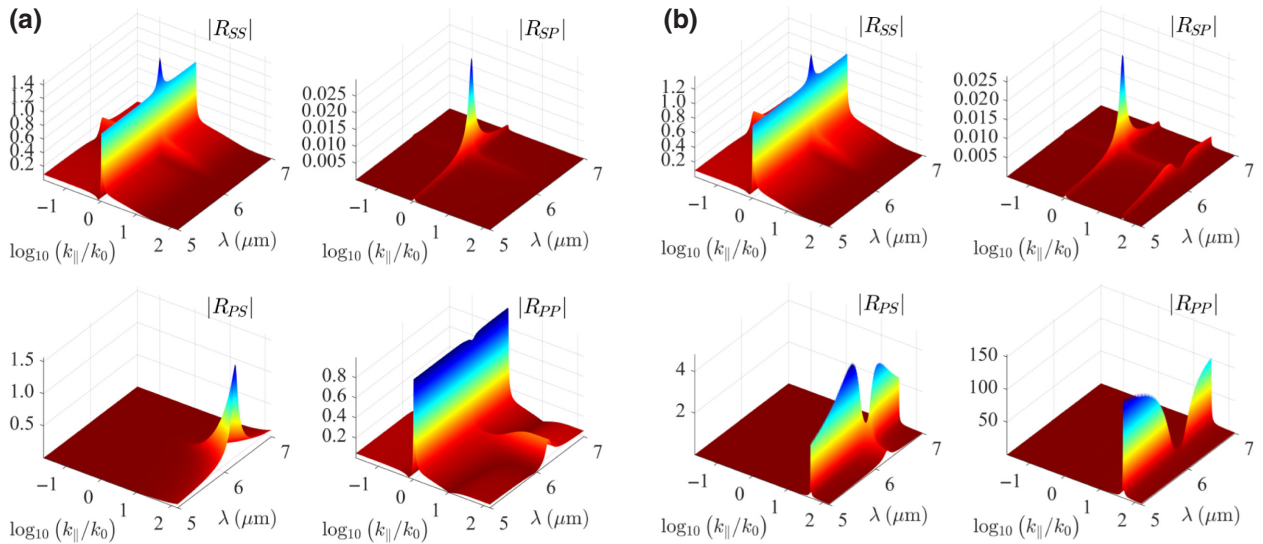


FIG. 6. Reflection and transmission coefficients of a chiral slab as functions of the normalized parallel wave vector  $k_\parallel/k_0$  and of the wavelength  $\lambda = 2\pi c/\omega$ , without (a) and with (b) a graphene sheet.

## 2. Field-parity analysis

We start our theoretical parity analysis from the slab field  $\mathbf{E}_\omega^{(S)}$  in Eq. (C4). After noting that the  $S$  and  $P$  unit vectors in Fourier space satisfy the relations

$$\begin{aligned}\mathbf{u}_S(\mathcal{R}\mathbf{k}_\parallel) &= -\mathcal{R}\mathbf{u}_S(\mathbf{k}_\parallel), \\ \mathbf{u}_P(\mathcal{R}\mathbf{k}_\parallel) &= \mathcal{R}\mathbf{u}_P(\mathbf{k}_\parallel),\end{aligned}\tag{C12}$$

and using the relation  $K_{z\tau}(\mathcal{R}\mathbf{k}_\parallel) = K_{z\tau}(\mathbf{k}_\parallel)$ , it is straightforward to prove that the mirror image of the slab field  $\mathbf{E}_\omega^{(S)}$  is

$$\mathbf{E}_\omega^{(S)'}(\mathbf{r}) = \int d^2\mathbf{k}_\parallel e^{i\mathbf{k}_\parallel \cdot \mathbf{r}_\parallel} \sum_{\sigma\tau} e^{i\sigma K_{z\tau} z} \left[ -n \frac{k_0}{i\sigma K_{z\tau}} \left( \frac{\kappa^2}{\sqrt{\varepsilon\kappa^2}} + \tau \right) \mathbf{u}_S + \left( \mathbf{u}_P - \frac{k_\parallel}{\sigma K_{z\tau}} \mathbf{e}_z \right) \right] U_\tau^{(\sigma)}(\mathcal{R}\mathbf{k}_\parallel).\tag{C13}$$

The mirror field in Eq. (C13) has the same structure as the slab field in Eq. (C4), the only difference being the minus sign in front of  $n$  so that, since all the other contributions depend only on  $\kappa^2$ , it is evident that the field  $\mathbf{E}_\omega^{(S)'}$  satisfies the second equation of Eq. (B4). In addition to explicitly providing a check of the full electromagnetic reflection invariance (as discussed in Appendix B), this reasoning clarifies that, due to the  $S$ - $P$  coupling in a chiral medium, the fields in two opposite enantiomers differ only in the relative sign of the  $S$  and  $P$  components and that taking the mirror image is equivalent to switching the sign of the  $S$  component.

We now evaluate the symmetric and antisymmetric parts, defined in Eq. (B5), of the fields produced by the slab in its achiral environment using the angular spectrum representations obtained in the above subsection. The mirror image of the incident field  $\mathbf{E}_\omega^{(i)}$  [see Eq. (C1)] is

$$\mathbf{E}_\omega^{(i)'} = \int d^2\mathbf{k}_\parallel e^{i\mathbf{k}_\parallel \cdot \mathbf{r}_\parallel} e^{ik_{1z}z} \left[ -U_S^{(i)}(\mathcal{R}\mathbf{k}_\parallel) \mathbf{u}_S + U_P^{(i)}(\mathcal{R}\mathbf{k}_\parallel) \left( \mathbf{u}_P - \frac{k_\parallel}{k_{1z}} \mathbf{e}_z \right) \right],\tag{C14}$$

where we use Eq. (C12), and consequently

$$\begin{aligned}\mathbf{E}_\omega^{(i)S} &= \int d^2\mathbf{k}_\parallel e^{i\mathbf{k}_\parallel \cdot \mathbf{r}_\parallel} e^{ik_{1z}z} \left[ U_S^{(i)A} \mathbf{u}_S + U_P^{(i)S} \left( \mathbf{u}_P - \frac{k_\parallel}{k_{1z}} \mathbf{e}_z \right) \right], \\ \mathbf{E}_\omega^{(i)A} &= \int d^2\mathbf{k}_\parallel e^{i\mathbf{k}_\parallel \cdot \mathbf{r}_\parallel} e^{ik_{1z}z} \left[ U_S^{(i)S} \mathbf{u}_S + U_P^{(i)A} \left( \mathbf{u}_P - \frac{k_\parallel}{k_{1z}} \mathbf{e}_z \right) \right],\end{aligned}\tag{C15}$$

where we introduce the symmetric and antisymmetric parts

$$\begin{aligned}U_j^{(i)S}(\mathbf{k}_\parallel) &= \frac{1}{2} \left[ U_j^{(i)}(\mathbf{k}_\parallel) + U_j^{(i)}(\mathcal{R}\mathbf{k}_\parallel) \right], \\ U_j^{(i)A}(\mathbf{k}_\parallel) &= \frac{1}{2} \left[ U_j^{(i)}(\mathbf{k}_\parallel) - U_j^{(i)}(\mathcal{R}\mathbf{k}_\parallel) \right]\end{aligned}\tag{C16}$$

of the  $j = \{S, P\}$  amplitudes. Such a decomposition directly provides a momentum-space characterization of incident MSFs, since the condition  $\mathbf{E}_\omega^{(i)A} = 0$  (see Appendix B) is equivalent to  $U_S^{(i)S} = U_P^{(i)A} = 0$ . In plain English, the incident field is a MSF if its  $S$  and  $P$  amplitudes are antisymmetric and symmetric, respectively, i.e.,

$$\begin{aligned}U_S^{(i)}(\mathbf{k}_\parallel) &= -U_S^{(i)}(\mathcal{R}\mathbf{k}_\parallel), \\ U_P^{(i)}(\mathbf{k}_\parallel) &= U_P^{(i)}(\mathcal{R}\mathbf{k}_\parallel).\end{aligned}\tag{C17}$$

Analogously, an incident field is a MAF if it has symmetric  $S$  and antisymmetric  $P$  spectral amplitudes. Since there is no constraint on the spectral amplitudes of the field in an achiral medium, the incident field can have definite parity (MSF and MAF) or not (IPF), in agreement with the discussion at the end of Appendix B. The mirror image of the reflected field  $\mathbf{E}_\omega^{(r)}$  [see the first equation of Eq. (C10)] is

$$\begin{aligned} \mathbf{E}_\omega^{(r)'} &= \int d^2\mathbf{k}_\parallel e^{i\mathbf{k}_\parallel \cdot \mathbf{r}_\parallel} e^{-ik_{1z}z} \left\{ - \left[ R_{SS}U_S^{(i)}(\mathcal{R}\mathbf{k}_\parallel) + nR_{SP}U_P^{(i)}(\mathcal{R}\mathbf{k}_\parallel) \right] \mathbf{u}_S \right. \\ &\quad \left. + \left[ nR_{PS}U_S^{(i)}(\mathcal{R}\mathbf{k}_\parallel) + R_{PP}U_P^{(i)}(\mathcal{R}\mathbf{k}_\parallel) \right] \left( \mathbf{u}_P + \frac{k_\parallel}{k_{1z}} \mathbf{e}_z \right) \right\}, \end{aligned} \quad (\text{C18})$$

where we use Eq. (C12) and the invariance of the reflection matrix  $R$  under the change  $\mathbf{k}_\parallel \rightarrow \mathcal{R}\mathbf{k}_\parallel$ , so that consequently

$$\begin{aligned} \mathbf{E}_\omega^{(r)S} &= \int d^2\mathbf{k}_\parallel e^{i\mathbf{k}_\parallel \cdot \mathbf{r}_\parallel} e^{-ik_{1z}z} \left[ \left( R_{SS}U_S^{(i)A} + nR_{SP}U_P^{(i)A} \right) \mathbf{u}_S + \left( nR_{PS}U_S^{(i)S} + R_{PP}U_P^{(i)S} \right) \left( \mathbf{u}_P + \frac{k_\parallel}{k_{1z}} \mathbf{e}_z \right) \right], \\ \mathbf{E}_\omega^{(r)A} &= \int d^2\mathbf{k}_\parallel e^{i\mathbf{k}_\parallel \cdot \mathbf{r}_\parallel} e^{-ik_{1z}z} \left[ \left( R_{SS}U_S^{(i)S} + nR_{SP}U_P^{(i)S} \right) \mathbf{u}_S + \left( nR_{PS}U_S^{(i)A} + R_{PP}U_P^{(i)A} \right) \left( \mathbf{u}_P + \frac{k_\parallel}{k_{1z}} \mathbf{e}_z \right) \right]. \end{aligned} \quad (\text{C19})$$

The most striking feature of Eq. (C19) is that  $\mathbf{E}_\omega^{(r)S}$  and  $\mathbf{E}_\omega^{(r)A}$  vanish separately only for very specific incident fields whose spectral amplitudes depend on the reflection coefficients  $R_{ij}$ , so that we conclude that the reflected field is generally an IPF. Analogous considerations hold for the transmitted field  $\mathbf{E}_\omega^{(t)}$ .

### 3. MOA

The situation where the incident field is a MSF is particularly relevant, since in this case, exploiting Eq. (C17), Eq. (C19) turn into

$$\begin{aligned} \mathbf{E}_\omega^{(r)S} &= \int d^2\mathbf{k}_\parallel e^{i\mathbf{k}_\parallel \cdot \mathbf{r}_\parallel} e^{-ik_{1z}z} \left[ R_{SS}U_S^{(i)} \mathbf{u}_S + R_{PP}U_P^{(i)} \left( \mathbf{u}_P + \frac{k_\parallel}{k_{1z}} \mathbf{e}_z \right) \right], \\ \mathbf{E}_\omega^{(r)A} &= n \int d^2\mathbf{k}_\parallel e^{i\mathbf{k}_\parallel \cdot \mathbf{r}_\parallel} e^{-ik_{1z}z} \left[ R_{SP}U_P^{(i)} \mathbf{u}_S + R_{PS}U_S^{(i)} \left( \mathbf{u}_P + \frac{k_\parallel}{k_{1z}} \mathbf{e}_z \right) \right], \end{aligned} \quad (\text{C20})$$

revealing that the reflected field necessarily is an IPF, since both its symmetric and its antisymmetric parts vanish if and only if the incident field vanishes. The antisymmetric part  $\mathbf{E}_\omega^{(r)A}$  contains only the mixing reflection coefficients  $R_{SP}$  and  $R_{PS}$ , which are produced entirely by the slab chirality (see the above subsection). We conclude that the generation of reflected and transmitted IPFs ( $\mathbf{E}_\omega^{(r)}$  and  $\mathbf{E}_\omega^{(t)}$ ) by a chiral slab in the presence of an incident MSF ( $\mathbf{E}_\omega^{(i)}$ ) is a genuine chiro-optical effect, which we refer to as MOA. As an additional remark, note that the  $S$  and  $P$  amplitudes of  $\mathbf{E}_\omega^{(r)A}$  in the second equation of Eq. (C20) are proportional to the  $P$  and  $S$  amplitudes, respectively, of  $\mathbf{E}_\omega^{(i)}$ . Such an  $S$ - $P$  dependency switch pertaining to MOA fully agrees with the very basic electric-magnetic coupling [see Eq. (A1)] lying at the heart of every chiro-optical effect, since the incident magnetic field of Eq. (C11) exhibits the same  $S$ - $P$  dependency switch as the antisymmetric part of the electric field.

Since the basic feature of MOA is the dissymmetry of the reflected (and transmitted) field, a local estimation of the efficiency of the process is provided by the ratio  $\Upsilon = |\mathbf{E}_\omega^A|/|\mathbf{E}_\omega^S|$  between the moduli of the antisymmetric and symmetric parts of the overall field  $\mathbf{E}_\omega = \mathbf{E}_\omega^{(i)} + \mathbf{E}_\omega^{(r)}$ . In

the substrate ( $z < 0$ ), it reduces to

$$\Upsilon = \frac{|\mathbf{E}_\omega^{(r)A}|}{|\mathbf{E}_\omega^{(i)} + \mathbf{E}_\omega^{(r)S}|}. \quad (\text{C21})$$

So, in order to observe efficient MOA, the antisymmetric part  $\mathbf{E}_\omega^{(r)A}$  should be enhanced at the expense of the symmetric part  $\mathbf{E}_\omega^{(r)S}$ . Since the mixing coefficient  $R_{PS}$  is prominent in the evanescent spectrum, where  $R_{SP}$  and  $R_{SS}$  are usually negligible (see Fig. 6), Eq. (C20) reveals that MOA is expected to be marked when the incident field has a prevalent  $S$  character with marked subwavelength features (so that, at the same time,  $R_{PS}U_S^{(i)}$  is enhanced and  $R_{PP}U_P^{(i)}$  is reduced while  $R_{SS}U_S^{(i)}$  remains small).

In Fig. 7(a), we sketch the phenomenology of MOA in order to highlight the dissymmetry of both the reflected and the transmitted fields. A particularly interesting feature of MOA is that if the same incident MSF  $\mathbf{E}_\omega^{(i)}$  is launched onto a second slab that is identical but filled with the opposite enantiomeric medium (with chirality parameter  $-\kappa$ ), the reflected and transmitted fields are  $\mathbf{E}_\omega^{(r)'}$  and  $\mathbf{E}_\omega^{(t)'}$ , i.e., they are the mirror images of the fields  $\mathbf{E}_\omega^{(r)}$  and  $\mathbf{E}_\omega^{(t)}$  produced

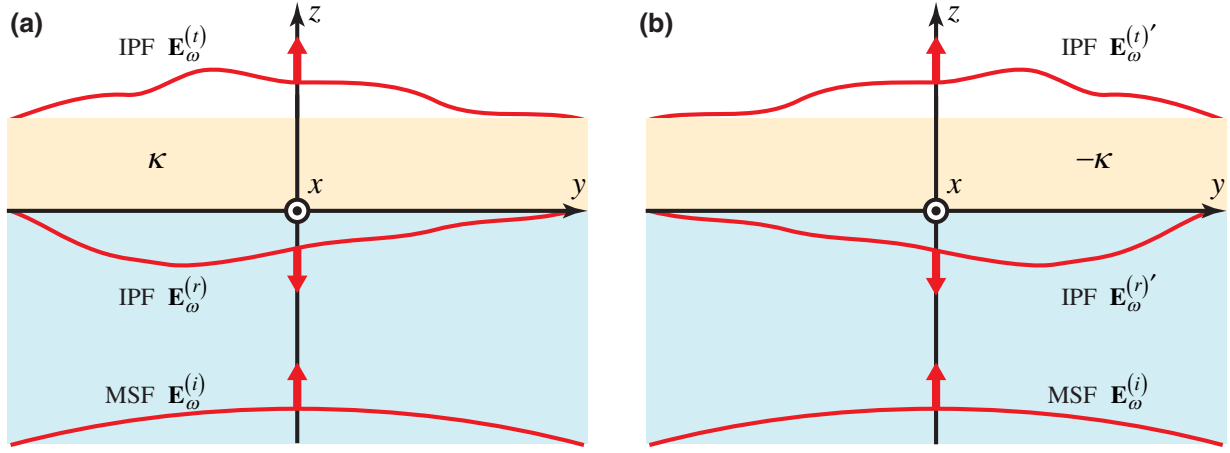


FIG. 7. (a) MOA: generation of reflected and transmitted IPFs by a chiral slab in the presence of an incident MSF. (b) The reflected and transmitted fields generated by the opposite enantiomeric slab (with chirality parameter  $-\kappa$ ) are the mirror images of the corresponding fields in (a).

by the first slab, as sketched in Fig. 7(b). Indeed, using the invariance of the  $R$  coefficients under the chirality reversal  $\kappa \rightarrow -\kappa$ , we obtain from Eq. (C20) that the symmetric and antisymmetric parts of the field reflected by the second slab are  $\mathbf{E}_\omega^{(r)S}$  and  $-\mathbf{E}_\omega^{(r)A}$ , the minus sign in the latter coming from the sign flip of  $n$  in the second equation of Eq. (C20), and these are precisely the symmetric and antisymmetric parts of the mirror-image field  $\mathbf{E}_\omega^{(r)'}$ . Such a MOA feature suggests viable enantiomeric sensing techniques where detection of the reflected and transmitted fields allows the discrimination of different enantiomerically pure samples or the measurement of the enantiomeric excess of a mixture.

#### APPENDIX D: MOA TRIGGERED BY FAST ELECTRONS

As discussed in the above appendix, the basic requirement for observing MOA is the excitation of a chiral slab by means of a MSF. In addition, since the  $S$ - $P$  coupling supporting MOA is particularly marked in the evanescent spectrum, it is highly desirable to choose an incident MSF with distinct subwavelength spatial features. The field generated by a fast electron meets both such requirements and hence is among the best available choices for the incident field. In addition, the electron velocity affects remarkably the mutual  $S$ - $P$  field content in momentum space, and hence can be exploited to efficiently tune the MOA phenomenology.

An electron of charge  $-e < 0$ , moving at a constant velocity  $v > 0$  along a trajectory  $\mathbf{r}^{(e)}(t) = vt\mathbf{e}_x - d\mathbf{e}_z$  in a transparent and unbounded dielectric of permittivity  $\varepsilon_1$ , generates a field [36] (for  $\omega > 0$ )

$$\begin{aligned} \mathbf{E}_\omega^{(e)} &= \frac{E_{\omega 0}}{\varepsilon_1 \beta^2 \gamma} e^{i(\omega/v)x} \left[ -K_1 \left( \frac{\omega R}{v\gamma} \right) \mathbf{e}_R + \frac{i}{\gamma} K_0 \left( \frac{\omega R}{v\gamma} \right) \mathbf{e}_x \right], \\ \mathbf{H}_\omega^{(e)} &= \frac{E_{\omega 0}}{Z_0 \beta \gamma} e^{i(\omega/v)x} \left[ -K_1 \left( \frac{\omega R}{v\gamma} \right) \mathbf{e}_\Phi \right], \end{aligned} \quad (\text{D1})$$

where  $E_{\omega 0} = eZ_0\omega/4\pi^2c$  is a field amplitude,  $\beta = v/c$ ,  $\gamma = 1/\sqrt{1 - \varepsilon_1\beta^2}$  is the Lorentz contraction factor, and  $K_n$  are modified Bessel functions of the second kind. Here cylindrical coordinates  $(R, \Phi)$  coaxial with the charge trajectory are introduced according to  $y = R \cos \Phi$ ,  $z = -d + R \sin \Phi$ , and  $\mathbf{e}_R = \nabla R$  and  $\mathbf{e}_\Phi = \mathbf{e}_z \times \mathbf{e}_R$  are the radial and azimuthal unit vectors. The field in Eq. (D1) is rotationally invariant around the electron trajectory, with the electric field lying in the radial  $Rx$  plane and the magnetic field being purely azimuthal. Such a field is a MSF, since it satisfies Eq. (B3), as can be straightforwardly checked by making use of the relations  $R(\mathcal{R}\mathbf{r}) = R(\mathbf{r})$ ,  $\mathbf{e}_R(\mathcal{R}\mathbf{r}) = \mathcal{R}\mathbf{e}_R(\mathbf{r})$ ,  $\mathbf{e}_\Phi(\mathcal{R}\mathbf{r}) = -\mathcal{R}\mathbf{e}_\Phi(\mathbf{r})$ , and  $\mathbf{e}_z = \mathcal{R}\mathbf{e}_z$ . In addition, the field displays marked subwavelength features in the sub-Cherenkov regime  $v < c/\sqrt{\varepsilon_1}$  (where  $\text{Im } \gamma = 0$ ), since it decays exponentially along the radial direction (through the modified Bessel functions) and does not provide electromagnetic radiation.

The evaluation of the electron field in momentum space is simplified by making use of the formalism of the Hertz vector  $\mathbf{\Pi}_\omega^{(e)}$ ,

$$\begin{aligned} \mathbf{\Pi}_\omega^{(e)} &= \frac{E_{\omega 0}}{ik_0^2 \varepsilon_1} e^{i(\omega/v)x} K_0 \left( \frac{\omega R}{v\gamma} \right) \mathbf{e}_x, \\ \begin{cases} \mathbf{E}_\omega^{(e)} = (k_0^2 \varepsilon_1 + \nabla \nabla \cdot) \mathbf{\Pi}_\omega^{(e)} \\ \mathbf{H}_\omega^{(e)} = \frac{k_0 \varepsilon_1}{iZ_0} \nabla \times \mathbf{\Pi}_\omega^{(e)} \end{cases}, \end{aligned} \quad (\text{D2})$$



since  $\Pi_\omega^{(e)}$  is everywhere along the  $x$  axis. By using the relation

$$K_0\left(h\sqrt{a^2+b^2}\right) = \frac{1}{2} \int_{-\infty}^{+\infty} dk e^{ika} \frac{e^{-\sqrt{h^2+k^2}|b|}}{\sqrt{h^2+k^2}} \quad (\text{D3})$$

for the modified Bessel function [45] and noting that  $(\omega^2/v^2\gamma^2) = -k_0^2\varepsilon_1 + (\omega^2/v^2)$ , we obtain from the first equation of Eq. (D2)

$$\Pi_\omega^{(e)} = \int d^2\mathbf{k}_\parallel e^{i\mathbf{k}_\parallel \cdot \mathbf{r}_\parallel} e^{ik_{1z}|z+d|} \frac{E_{\omega 0}}{2k_0^2\varepsilon_1 k_{1z}} \delta\left(k_x - \frac{\omega}{v}\right) \mathbf{e}_x, \quad (\text{D4})$$

where the delta function is introduced to select the longitudinal wave number  $\omega/v$ . Evaluating the electric field from such a Fourier representation of the Hertz vector by using the first equation in the right system of Eq. (D2), we get

$$\begin{cases} \nabla \cdot \mathbf{E}_\omega^{(e)} = \frac{1}{\varepsilon_0\varepsilon_1} \rho_\omega^{(e)} \\ \nabla \cdot \mathbf{H}_\omega^{(e)} = 0 \\ \nabla \times \mathbf{E}_\omega^{(e)} = i\omega\mu_0\mathbf{H}_\omega^{(e)} \\ \nabla \times \mathbf{H}_\omega^{(e)} = -i\omega\varepsilon_0\varepsilon_1\mathbf{E}_\omega^{(e)} + \mathbf{J}_\omega^{(e)} \end{cases}, \quad \begin{cases} \rho_\omega^{(e)} = -\frac{e}{2\pi|v|} e^{i(\omega/v)x} \delta(y) \delta(z+d) \\ \mathbf{J}_\omega^{(e)} = -\frac{e}{2\pi} e^{i(\omega/v)x} \delta(y) \delta(z+d) \mathbf{e}_x \end{cases}.$$

However, in both of the regions  $z > -d$  and  $z < -d$ ,  $\rho_\omega^{(e)}$  and  $\mathbf{J}_\omega^{(e)}$  vanish, and the field locally admits an angular spectrum representation, which depends on the region.

Suppose now that the electron travels in the substrate of the setup reported in Fig. 8 in the presence of the chiral slab. The field in Eq. (D1) satisfies the Maxwell equations in  $z < 0$  and, along the stripe  $-d < z < 0$ , its Fourier representation in Eq. (D5) turns into an angular spectrum representation whose structure coincides with that of Eq. (C1) (since  $z+d > 0$ ). As a consequence, the electron is the source of a field impinging on the chiral slab, whose spectral amplitudes are

$$\begin{aligned} U_S^{(ei)} &= E_{\omega 0} \frac{e^{ik_{1z}d}}{2k_\parallel} \left( -\frac{k_y}{k_{1z}} \right) \delta\left(k_x - \frac{\omega}{v}\right), \\ U_P^{(ei)} &= E_{\omega 0} \frac{e^{ik_{1z}d}}{2k_\parallel} \left( \frac{k_{1z}}{\beta k_0\varepsilon_1} \right) \delta\left(k_x - \frac{\omega}{v}\right), \end{aligned} \quad (\text{D7})$$

which manifestly satisfy Eq. (C17), as expected since the electron field is a MSF. Therefore the fast electron triggers MOA, whose efficiency is magnified by the evanescent character of the impinging field in the sub-Cherenkov regime  $\beta < (1/\sqrt{\varepsilon_1})$ . The reflected field

$$\begin{aligned} \mathbf{E}_\omega^{(e)} &= \int d^2\mathbf{k}_\parallel e^{i\mathbf{k}_\parallel \cdot \mathbf{r}_\parallel} e^{ik_{1z}|z+d|} \frac{E_{\omega 0}}{2k_\parallel} \delta\left(k_x - \frac{\omega}{v}\right) \\ &\times \left[ -\frac{k_y}{k_{1z}} \mathbf{u}_S + \frac{k_{1z}}{\beta k_0\varepsilon_1} \left( \mathbf{u}_P - \text{sign}(z+d) \frac{k_\parallel}{k_{1z}} \mathbf{e}_z \right) \right]. \end{aligned} \quad (\text{D5})$$

Note that, due to the delta function, the longitudinal wave number is

$$k_{1z} = i\sqrt{\frac{\omega^2}{v^2\gamma^2} + k_y^2}, \quad (\text{D6})$$

so that the field spectrum is entirely evanescent, and  $|z+d|$  ensures that the field fades both for  $z < -d$  and for  $z > -d$ .

Equation (D5) is not an angular spectrum representation, due to the presence of the modulus and sign of  $z+d$ . This is a consequence of the fact that the electron field is not source-free, since it satisfies the Maxwell equations with the charge and current densities  $\rho_\omega^{(e)}$  and  $\mathbf{J}_\omega^{(e)}$  associated with the moving electron, i.e.,

$\mathbf{E}_\omega^{(er)}$  is an IPF, and its symmetric and antisymmetric parts can be evaluated by inserting Eq. (D7) into Eq. (C20); thus we obtain

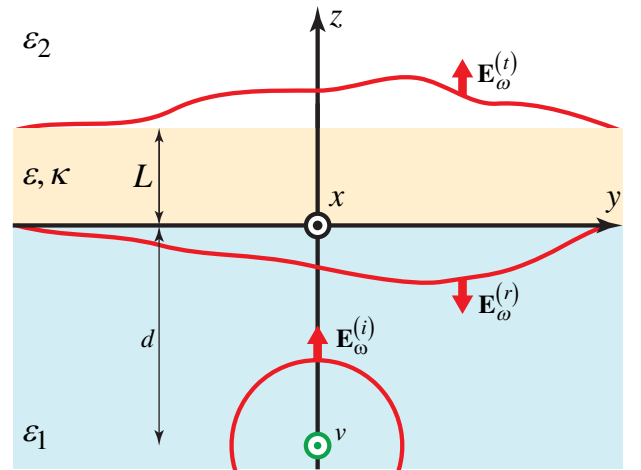


FIG. 8. MOA triggered by a fast electron interacting with a chiral slab in an aloof configuration. The electron provides an incident MSF triggering the reflection and transmission of IPFs by the slab.

$$\begin{aligned}\mathbf{E}_\omega^{(er)S} &= e^{i(\omega/v)x} \int_{-\infty}^{+\infty} dk_y e^{ik_y y} \left\{ e^{ik_{1z}z} \left[ \tilde{U}_S^{(r)A} \mathbf{u}_S + \tilde{U}_P^{(r)S} \left( \mathbf{u}_P + \frac{k_{\parallel}}{k_{1z}} \mathbf{e}_z \right) \right] \right\}_{k_x=\omega/v}, \\ \mathbf{E}_\omega^{(er)A} &= e^{i(\omega/v)x} \int_{-\infty}^{+\infty} dk_y e^{ik_y y} \left\{ e^{ik_{1z}z} \left[ \tilde{U}_S^{(r)S} \mathbf{u}_S + \tilde{U}_P^{(r)A} \left( \mathbf{u}_P + \frac{k_{\parallel}}{k_{1z}} \mathbf{e}_z \right) \right] \right\}_{k_x=\omega/v},\end{aligned}\quad (\text{D8})$$

where

$$\begin{aligned}\tilde{U}_S^{(r)A} &= E_{\omega 0} \left[ \frac{e^{ik_{1z}d}}{2k_{\parallel}} \left( -\frac{k_y}{k_{1z}} R_{SS} \right) \right]_{k_x=\omega/v}, & \tilde{U}_P^{(r)S} &= E_{\omega 0} \left[ \frac{e^{ik_{1z}d}}{2k_{\parallel}} \left( \frac{k_{1z}}{\beta k_0 \varepsilon_1} R_{PP} \right) \right]_{k_x=\omega/v}, \\ \tilde{U}_S^{(r)S} &= E_{\omega 0} \left[ \frac{e^{ik_{1z}d}}{2k_{\parallel}} \left( n \frac{k_{1z}}{\beta k_0 \varepsilon_1} R_{SP} \right) \right]_{k_x=\omega/v}, & \tilde{U}_P^{(r)A} &= E_{\omega 0} \left[ \frac{e^{ik_{1z}d}}{2k_{\parallel}} \left( -n \frac{k_y}{k_{1z}} R_{PS} \right) \right]_{k_x=\omega/v},\end{aligned}\quad (\text{D9})$$

are the symmetric and antisymmetric parts of the  $S$  and  $P$  amplitudes of the reflected field.

In Fig. 9, we plot the four spectral amplitudes in Eq. (D9) as functions of the normalized wave number  $k_y/k_0$  (for  $k_y > 0$ ) and the wavelength  $\lambda$ , for different parameters  $d, \beta$  of an electron interacting with the same substrate, slab, and superstrate (with and without graphene) as those considered in Fig. 6. In Figs. 9(a) and 9(b), the graphene is absent, and the electron trajectory is located at  $d = 0.01 \mu\text{m}$  away from the chiral-slab interface, with  $\beta = 0.05$  [Fig. 9(a)] and  $\beta = 0.8$  [Fig. 9(b)]. In the first case of lower electron energy [Fig. 9(a)], the amplitude  $\tilde{U}_P^{(r)S}$  is dominant, and hence the antisymmetric part  $\mathbf{E}_\omega^{(r)A}$  is small compared with  $\mathbf{E}_\omega^{(r)S}$ , so that the MOA efficiency is expected to be low. On the other hand, in the second case of higher electron energy [Fig. 9(b)],  $\tilde{U}_P^{(r)S}$  is considerably smaller than in the previous case and is comparable to  $\tilde{U}_P^{(r)A}$  (while  $\tilde{U}_S^{(r)A}$  and  $\tilde{U}_S^{(r)S}$  are comparable), so that the MOA efficiency is higher than in the case of Fig. 9(a). We conclude that the MOA efficiency increases when the electron energy is increased, and this agrees with the discussion in Sec. 3, since the  $S/P$  amplitude ratio of the electron (incident) field [see Eq. (D7)],

$$\left| \frac{U_S^{(ei)}}{U_P^{(ei)}} \right| = \frac{\beta \varepsilon_1}{(1/\beta^2 - \varepsilon_1) (k_0/|k_y|) + (|k_y|/k_0)}, \quad (\text{D10})$$

is an increasing function of  $\beta$ . In Figs. 9(c) and 9(d), the graphene is present, and the electron trajectory is located at  $d = 0.03 \mu\text{m}$  away from the chiral-slab interface, with  $\beta = 0.05$  [Fig. 9(c)] and  $\beta = 0.8$  [Fig. 9(d)]. The same reasoning as in the graphene-free situations of Figs. 9(a) and 9(b) leads to the conclusion that the MOA efficiency is higher at larger electron energy and also benefits from the graphene plasmon resonance.

The setup encompassing a graphene sheet is, however, even more interesting, since the combination of the graphene plasmon resonance and the field dissymmetry triggers a near-field interferometric phenomenon, which can further increase the MOA efficiency. Figures 9(c) and 9(d) manifestly signal the graphene plasmon resonance through a peak centered at a specific parallel wave number  $k_y = k_p(\lambda)$ . Now the resonance corresponds to the minimum of the determinant of the matrix  $\underline{M}$  in the first equation of Eq. (C8), which is invariant under the change  $\mathbf{k}_{\parallel} \rightarrow -\mathcal{R}\mathbf{k}_{\parallel}$ , so that  $k_y = k_p$  and  $k_y = -k_p$  contribute equivalently to the graphene plasmon resonance. If we neglect for simplicity the width of the resonance peaks and retain in Eq. (D8) only the contributions from the wave numbers  $k_y = k_p$  and  $k_y = -k_p$ , we get

$$\begin{aligned}\mathbf{E}_\omega^{(r)S} &\cong \Delta k \left\{ e^{ik_x x} e^{ik_{1z}z} \left[ \tilde{U}_S^{(r)A} \mathbf{u}_S + \tilde{U}_P^{(r)S} \left( \mathbf{u}_P + \frac{k_{\parallel}}{k_{1z}} \mathbf{e}_z \right) \right] \right\}_{\mathbf{k}_{\parallel}=(\omega/v)\mathbf{e}_x+k_p\mathbf{e}_y} & 2 \cos(k_p y), \\ \mathbf{E}_\omega^{(r)A} &\cong \Delta k \left\{ e^{ik_x x} e^{ik_{1z}z} \left[ \tilde{U}_S^{(r)S} \mathbf{u}_S + \tilde{U}_P^{(r)A} \left( \mathbf{u}_P + \frac{k_{\parallel}}{k_{1z}} \mathbf{e}_z \right) \right] \right\}_{\mathbf{k}_{\parallel}=(\omega/v)\mathbf{e}_x+k_p\mathbf{e}_y} & 2i \sin(k_p y),\end{aligned}\quad (\text{D11})$$

where  $\Delta k$  is the resonance width, and the symmetry and antisymmetry of the integrands of  $\mathbf{E}_\omega^{(r)S}$  and  $\mathbf{E}_\omega^{(r)A}$ , respectively, are exploited [see Eqs. (C12) and (D9)]. We conclude that interference between counterpropagating graphene plasmon polaritons with parallel wave numbers  $k_y = k_p$  and  $k_y = -k_p$  endows the symmetric and the antisymmetric parts of the reflected field with cosinusoidal and sinusoidal profiles, respectively, along the  $y$  axis whose spatial period is  $2\pi/k_p$ . What

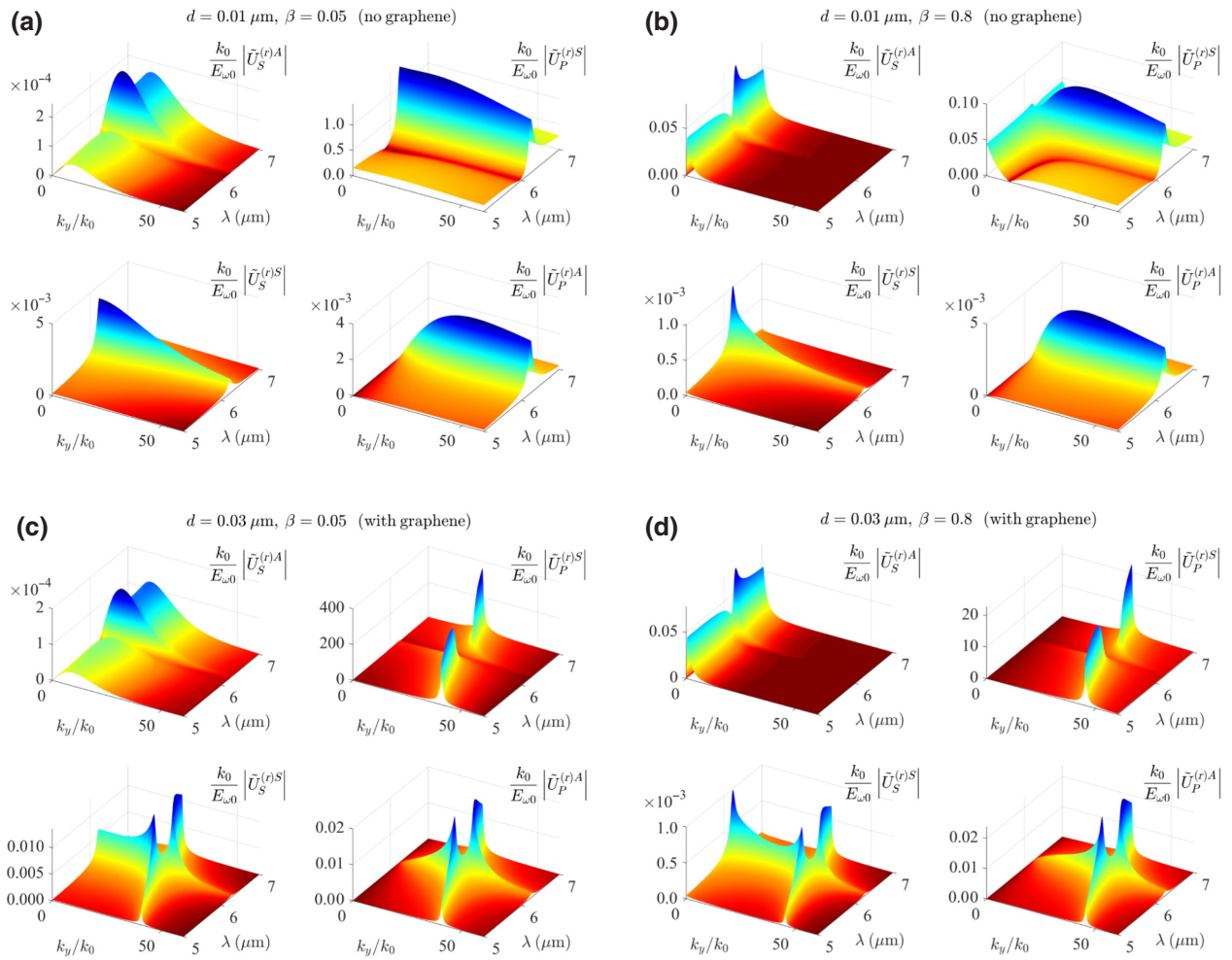


FIG. 9. Symmetric and antisymmetric parts of the  $S$  and  $P$  amplitudes of the IPF reflected by a chiral slab interacting with an aloof electron. The normalized amplitudes are plotted as functions of the normalized wave number  $k_y/k_0$  (for  $k_y > 0$ ) and the wavelength  $\lambda$ , for different parameters  $d, \beta$  of the electron interacting with the same substrate, slab, and superstrate (with and without graphene) considered in Fig. 6.

is remarkable here is that at the points where  $|\mathbf{E}_\omega^{(r)A}|$  is maximum,  $|\mathbf{E}_\omega^{(r)S}|$  is minimum, and consequently the dissymmetry factor  $\Upsilon$  of Eq. (C21) benefits from an additional local enhancement, thus raising the MOA efficiency.

### APPENDIX E: MOA DETECTION THROUGH CATHODOLUMINESCENCE

MOA accompanying the excitation of a chiral slab by means of a fast electron is intrinsically a near-field phenomenon (as discussed above), and hence detection techniques for it can be borrowed from a number of currently available nanophotonic strategies. In this paper, we consider the standard nanoantenna technique, where a nanoparticle in the substrate experiences the near field and outcouples radiation, which in turn is detectable in the superstrate as cathodoluminescence. By placing the nanoparticle at two symmetric positions alongside

the electron trajectory, two unequal cathodoluminescence signals can be collected, their difference amounting to MOA detection.

We consider a plasmonic nanoparticle of radius  $a$  lying upon the graphene sheet with its center located at  $\mathbf{r}_{\text{NP}} =$

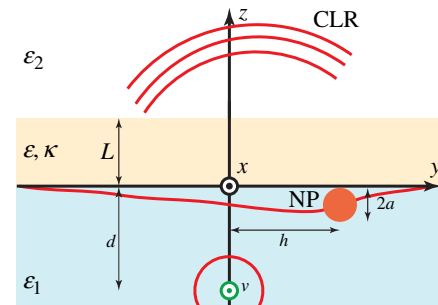


FIG. 10. Cathodoluminescence radiation (CLR) produced by a nanoparticle in the substrate.

$h\mathbf{e}_y - a\mathbf{e}_z$  in the substrate, as sketched in Fig. 10. The dielectric permittivity of the nanoparticle is described by the Drude model  $\varepsilon_{\text{NP}}(\omega) = 1 - \omega_p^2/(\omega^2 + i\omega\Gamma)$ , which accurately describes transparent conductors with a plasma frequency  $\omega_p$  in the midinfrared. Since the radius  $a$  is much smaller than midinfrared wavelengths and the near field does not self-consistently display large field gradients, we make use of the electrostatic (nonretarded) approximation here, where the nanoparticle is modeled by a point dipole located at  $\mathbf{r}_{\text{NP}}$  whose dipole moment (in the frequency domain) is  $\mathbf{p}_\omega = \alpha \mathbf{E}_\omega^{(\text{ext})}$ , where  $\mathbf{E}_\omega^{(\text{ext})}$  is the field experienced by the dipole (without self-field) and  $\alpha = 4\pi\varepsilon_0\varepsilon_1 a^3 [(\varepsilon_{\text{NP}} - \varepsilon_1)/(\varepsilon_{\text{NP}} + 2\varepsilon_1)]$  is the well-known polarizability of a sphere. The field produced by the dipole in the substrate ( $z < 0$ ) is

$$\mathbf{E}_\omega^{(p)} = (k_0^2\varepsilon_1 + \nabla\nabla\cdot) \left( \frac{1}{4\pi\varepsilon_0\varepsilon_1} \frac{e^{ik_0\sqrt{\varepsilon_1}|\mathbf{r}-\mathbf{r}_{\text{NP}}|}}{|\mathbf{r}-\mathbf{r}_{\text{NP}}|} \mathbf{p}_\omega \right), \quad (\text{E1})$$

which, after using the Weyl representation of a spherical wave

$$\frac{e^{ik_0\sqrt{\varepsilon_1}r}}{r} = \frac{i}{2\pi} \int d^2\mathbf{k}_\parallel e^{i\mathbf{k}_\parallel\cdot\mathbf{r}_\parallel} \frac{e^{ik_{1z}|z|}}{k_{1z}}, \quad (\text{E2})$$

can be cast as

$$\mathbf{E}_\omega^{(p)} = \int d^2\mathbf{k}_\parallel e^{i\mathbf{k}_\parallel\cdot\mathbf{r}_\parallel} e^{ik_z|z+a|} \frac{ik_0 e^{-ik_y h}}{8\pi^2\varepsilon_0\varepsilon_1} \left[ \left( \frac{k_0\varepsilon_1}{k_{1z}} \mathbf{u}_S \right) \cdot \mathbf{p}_\omega \mathbf{u}_S \right. \quad (\text{E3})$$

$$\left. + \left( \frac{k_{1z}}{k_0} \mathbf{u}_P - \frac{k_\parallel}{k_0} \text{sgn}(z+a) \mathbf{e}_z \right) \cdot \mathbf{p}_\omega \left( \mathbf{u}_P - \frac{k_\parallel}{k_{1z}} \text{sgn}(z+a) \mathbf{e}_z \right) \right]. \quad (\text{E4})$$

In analogy with the electron field of Eq. (D5), the Fourier representation of the dipole field in Eq. (E3) reduces to an angular spectrum representation of the form of Eq. (C1) along the stripe  $-a < z < 0$ , from which its  $S$  and  $P$  amplitudes are

$$U_S^{(pi)} = \frac{ik_0}{8\pi^2\varepsilon_0\varepsilon_1} e^{-ik_y h} e^{ik_{1z}a} \left( \frac{k_0\varepsilon_1}{k_{1z}} \mathbf{u}_S \right) \cdot \mathbf{p}_\omega, \quad (\text{E5})$$

$$U_P^{(pi)} = \frac{ik_0}{8\pi^2\varepsilon_0\varepsilon_1} e^{-ik_y h} e^{ik_{1z}a} \left( \frac{k_{1z}}{k_0} \mathbf{u}_P - \frac{k_\parallel}{k_0} \mathbf{e}_z \right) \cdot \mathbf{p}_\omega.$$

Inserting Eq. (E5) into Eq. (C10), we obtain the reflected ( $pr$ ) and transmitted ( $pt$ ) dipole fields

$$\begin{aligned} \mathbf{E}_\omega^{(pr)} &= G^{(pr)} \mathbf{p}_\omega \quad (z < 0), \\ \mathbf{E}_\omega^{(pt)} &= G^{(pt)} \mathbf{p}_\omega \quad (z > L), \end{aligned} \quad (\text{E6})$$

where, using the dyadic notation  $(\mathbf{ab})\mathbf{c} = (\mathbf{b} \cdot \mathbf{c}) \mathbf{a}$ ,

$$\begin{aligned} G^{(pr)} &= \frac{ik_0}{8\pi^2\varepsilon_0\varepsilon_1} \int d^2\mathbf{k}_\parallel e^{i\mathbf{k}_\parallel\cdot\mathbf{r}_\parallel} e^{-ik_{1z}z} e^{-ik_y h} e^{ik_{1z}a} \left\{ \left[ R_{SS} \mathbf{u}_S + nR_{PS} \left( \mathbf{u}_P + \frac{k_\parallel}{k_{1z}} \mathbf{e}_z \right) \right] \left( \frac{k_0\varepsilon_1}{k_{1z}} \mathbf{u}_S \right) \right. \\ &\quad \left. + \left[ nR_{SP} \mathbf{u}_S + R_{PP} \left( \mathbf{u}_P + \frac{k_\parallel}{k_{1z}} \mathbf{e}_z \right) \right] \left( \frac{k_{1z}}{k_0} \mathbf{u}_P - \frac{k_\parallel}{k_0} \mathbf{e}_z \right) \right\}, \\ G^{(pt)} &= \frac{ik_0}{8\pi^2\varepsilon_0\varepsilon_1} \int d^2\mathbf{k}_\parallel e^{i\mathbf{k}_\parallel\cdot\mathbf{r}_\parallel} e^{ik_{2z}(z-L)} e^{-ik_y h} e^{ik_{1z}a} \left\{ \left[ T_{SS} \mathbf{u}_S + nT_{PS} \left( \mathbf{u}_P - \frac{k_\parallel}{k_{2z}} \mathbf{e}_z \right) \right] \left( \frac{k_0\varepsilon_1}{k_{1z}} \mathbf{u}_S \right) \right. \\ &\quad \left. + \left[ nT_{SP} \mathbf{u}_S + T_{PP} \left( \mathbf{u}_P - \frac{k_\parallel}{k_{2z}} \mathbf{e}_z \right) \right] \left( \frac{k_{1z}}{k_0} \mathbf{u}_P - \frac{k_\parallel}{k_0} \mathbf{e}_z \right) \right\}. \end{aligned} \quad (\text{E7})$$

The dyadics  $G^{(pr)}$  and  $G^{(pt)}$  fully describe the electromagnetic response of the chiral slab in the achiral environment and may be easily evaluated numerically in the near field. In addition, their Fourier representations are directly suitable for a far-field analysis (see below). In order to evaluate the dipole moment  $\mathbf{p}_\omega$  induced by the fast electron and the chiral slab, note that the nanoparticle experiences an external field

$$\mathbf{E}_\omega^{(\text{ext})} = \left[ \mathbf{E}_\omega^{(e)} + \mathbf{E}_\omega^{(er)} + \mathbf{E}_\omega^{(pr)} \right]_{\mathbf{r}=\mathbf{r}_{\text{NP}}}, \quad (\text{E8})$$

so that, using the nanoparticle polarizability  $\alpha$  and the first equation of Eq. (E6), we get

$$\mathbf{p}_\omega = \left\{ \left[ \frac{1}{\alpha} I - G^{(pr)} \right]^{-1} \left( \mathbf{E}_\omega^{(e)} + \mathbf{E}_\omega^{(er)} \right) \right\}_{\mathbf{r}=\mathbf{r}_{\text{NP}}}, \quad (\text{E9})$$

where  $I$  is the identity dyadic. Such an equation reveals that the nanoparticle provides an ideal tool for probing MOA, since its dipole moment depends linearly on the total electron field  $\mathbf{E}_\omega^{(e)} + \mathbf{E}_\omega^{(er)}$  evaluated at the center of the nanoparticle.



Since we are considering the sub-Cherenkov regime and the aloof electron does not produce transition radiation, the cathodoluminescence radiation is due only to the nanoparticle. Radiation detection is usually performed in the superstrate, and consequently we focus on  $\mathbf{E}_\omega^{(pt)}$ . After introducing polar coordinates  $x = r \sin \theta \cos \varphi$ ,  $y = r \sin \theta \sin \varphi$ ,  $z = r \cos \theta$  together with their coordinate unit vectors  $\mathbf{e}_r$ ,  $\mathbf{e}_\theta$ ,  $\mathbf{e}_\varphi$  and using the relation

$$\int d^2 \mathbf{k}_\parallel e^{i \mathbf{k}_\parallel \cdot \mathbf{r}_\parallel} e^{i k_{2z} z} F(\mathbf{k}_\parallel) = \frac{e^{i k_0 \sqrt{\varepsilon_2} r}}{r} \left( \frac{2\pi}{i} \right) F \left( k_0 \sqrt{\varepsilon_2} \sin \theta \frac{\mathbf{r}_\parallel}{r_\parallel} \right) k_0 \sqrt{\varepsilon_2} \cos \theta, \quad (\text{E10})$$

which provides the leading order of the asymptotic expansion for  $k_0 r \rightarrow \infty$  and  $\cos \theta > 0$  of the Fourier integral, we obtain the usual far-field expression for  $\mathbf{E}_\omega^{(pt)}$  from the second equations of Eqs. (E6) and (E7),

$$\mathbf{E}_\omega^{(pt)} = \frac{e^{i k_0 \sqrt{\varepsilon_2} r}}{k_0 r} \mathbf{f}(\theta, \varphi), \quad (\text{E11})$$

where

$$\begin{aligned} \mathbf{f} &= \left[ \cos \theta (T_{SS} E_S + n T_{SP} E_P) \mathbf{e}_\varphi + (n T_{PS} E_S + T_{PP} E_P) \mathbf{e}_\theta \right]_{k_\parallel = k_0 \sqrt{\varepsilon_2} \sin \theta}, \\ \begin{pmatrix} E_S \\ E_P \end{pmatrix} &= \frac{k_0^3 \sqrt{\varepsilon_2}}{4\pi \varepsilon_0 \sqrt{\varepsilon_1}} e^{-i k_0 [\sqrt{\varepsilon_2} L \cos \theta + \sqrt{\varepsilon_2} h \sin \theta \sin \varphi - a \sqrt{\varepsilon_1 - \varepsilon_2} \sin^2 \theta]} \\ &\times \begin{pmatrix} -\sin \varphi p_{\omega x} + \cos \varphi p_{\omega y} \\ \sqrt{1 - (\varepsilon_2/\varepsilon_1) \sin^2 \theta} \\ \sqrt{1 - (\varepsilon_2/\varepsilon_1) \sin^2 \theta} (\cos \varphi p_{\omega x} + \sin \varphi p_{\omega y}) - \sqrt{(\varepsilon_2/\varepsilon_1)} \sin \theta p_{\omega y} \end{pmatrix}. \end{aligned} \quad (\text{E12})$$

The total energy emitted by cathodoluminescence per incoming electron is

$$\begin{aligned} U &= \int_{-\infty}^{\infty} dt \int d\Omega r^2 \mathbf{e}_r \cdot [\mathbf{E}(\mathbf{r}, t) \times \mathbf{H}(\mathbf{r}, t)] \\ &= \int_0^{\infty} d\lambda \left( \frac{hc}{\lambda} \right) \int d\Omega \frac{dN}{d\Omega d\lambda}, \end{aligned} \quad (\text{E13})$$

where  $hc/\lambda$  is the photon energy quantum and  $dN/d\Omega d\lambda = (4\pi/\hbar\lambda) r^2 \mathbf{e}_r \cdot \text{Re}(\mathbf{E}_\omega \times \mathbf{H}_\omega^*)$  is the number of photons emitted per incoming electron, per unit of solid angle of emission and per unit of photon wavelength. By using Eq. (E11) and the far-field relation  $\mathbf{H}_\omega^{(pt)} = (\sqrt{\varepsilon_2}/Z_0) \mathbf{e}_r \times \mathbf{E}_\omega^{(pt)}$ , we get in the superstrate  $dN/d\Omega d\lambda = (\lambda \sqrt{\varepsilon_2}/\pi \hbar Z_0) |\mathbf{f}|^2$ , which, after integration over the solid angle  $\cos \theta > 0$ , yields

$$\Gamma = \frac{\lambda \sqrt{\varepsilon_2}}{\pi \hbar Z_0} \int_{\cos \theta > 0} d\Omega |\mathbf{f}|^2, \quad (\text{E14})$$

i.e., the number of photons emitted per incoming electron in the superstrate per unit photon wavelength.

Suppose now that two symmetric situations are considered where the same nanoparticle is placed at  $\mathbf{r}_{\text{NP}}^{(+)} = h\mathbf{e}_y - a\mathbf{e}_z$  and at  $\mathbf{r}_{\text{NP}}^{(-)} = -h\mathbf{e}_y - a\mathbf{e}_z$ . Because of MOA, the corresponding nanoparticle dipole moments  $\mathbf{p}_\omega^{(+)}$  and  $\mathbf{p}_\omega^{(-)}$  are necessarily different, and consequently the associated

cathodoluminescence signals  $\Gamma(h)$  and  $\Gamma(-h)$  are different as well. Therefore the dissymmetry factor

$$\delta\Gamma(h) = -2 \frac{\Gamma(h) - \Gamma(-h)}{\Gamma(h) + \Gamma(-h)}, \quad (\text{E15})$$

effectively provides a quantitative measurement of the MOA efficiency and chiral sensing.

From an experimental perspective, the target is to measure the profile of  $\Gamma(h)$ , its asymmetry providing chiral sensing. This can be done in different ways, either by mechanically moving the sample or by physically shifting the electron beam with static electric fields. Achieving perfect electron-beam collinearity should not be a critical issue, since, for the energies and wavelengths considered here, the point-dipole response of the nanoparticle is fully adequate.

## APPENDIX F: INFRARED LOCAL OPTICAL RESPONSE OF GRAPHENE

At infrared frequencies, the optical response of graphene is dominated by the conical band structure  $\mathcal{E} = \pm v_F |\mathbf{p}_\parallel|$  around the two Dirac points of the first Brillouin zone, where  $v_F \approx 9 \times 10^5$  m/s is the Fermi velocity, and  $\mathcal{E}$  and  $\mathbf{p}_\parallel$  are the electron energy and momentum, respectively. In the present investigation, we focus mainly on the infrared range of wavelengths  $5 \mu\text{m} < \lambda < 20 \mu\text{m}$ . While in undoped graphene the Fermi energy lies at the Dirac

points, injection of charge carriers through electrical gating [46] or chemical doping [47] can efficiently shift the Fermi level up to  $E_F \approx 1$  eV owing to the conical dispersion and the 2D electron confinement. The response of graphene to photons of energy  $\hbar\omega$  and in-plane momentum  $\hbar\mathbf{k}_\parallel$  is described by the surface conductivity  $\sigma_G(\mathbf{k}_\parallel, \omega)$ , which is generally affected by both intraband and interband electron dynamics. The dependence of  $\sigma_G$  on  $\mathbf{k}_\parallel$  physically arises from the excitation of electron-hole pairs and generally yields unwanted absorption (Landau damping) and nonlocal effects. However, if

$$\frac{k_\parallel}{k_F} < \frac{\hbar\omega}{E_F} < 2 - \frac{k_\parallel}{k_F}, \quad (\text{F1})$$

where  $k_F = E_F/\hbar v_F$  is the Fermi wave number, the photon momentum is too small to trigger intraband transitions, and interband transitions are forbidden by the Pauli exclusion principle [48]. When graphene is interacting with photons satisfying Eq. (F1), nonlocal effects can be neglected, and it displays a marked metallike behavior with a long relaxation time  $\tau = \mu E_F / ev_F^2$ , where  $\mu$  is the electron mobility, which, conversely to noble metals, can reach the picosecond time scale at moderate doping and purity (which affect the electron mobility) [49]. In such a local regime, the random-phase approximation provides for the conductivity of graphene the integral expression

$$\sigma_G(\omega) = \frac{-ie^2}{\pi \hbar^2(\omega + i/\tau)} \int_{-\infty}^{+\infty} d\mathcal{E} \times \left\{ |\mathcal{E}| \frac{\partial f_\mathcal{E}}{\partial \mathcal{E}} + \frac{\text{sign}(\mathcal{E})}{1 - 4\mathcal{E}^2/[\hbar(\omega + i/\tau)]^2} f_\mathcal{E} \right\}, \quad (\text{F2})$$

where  $f_\mathcal{E} = \{\exp[(\mathcal{E} - E_F)/k_B T] + 1\}^{-1}$  is the Fermi function ( $k_B$  is the Boltzmann constant and  $T$  is the temperature). In our analysis, we focus on photon-graphene interactions satisfying Eq. (F1), and accordingly we model the surface conductivity of graphene by means of Eq. (F2).

It is worth noting that, in the regime where the Fermi energy is greater than the photon energy ( $E_F > \hbar\omega$ ), Eq. (F1) can be cast as

$$k_\parallel < \left(\frac{c}{v_F}\right) k_0 \simeq 333k_0, \quad (\text{F3})$$

which specifies the wave-vector range of those photons that do not trigger nonlocal effects at frequency  $\omega$ .

[1] P. Curie, Sur la symétrie dans les phénomènes physiques, symétrie d'un champ électrique et d'un champ magnétique, *J. Phys. Theor. Appl.* **3**, 393 (1894).

- [2] F. D. M. Haldane and S. Raghu, Possible Realization of Directional Optical Waveguides in Photonic Crystals with Broken Time-Reversal Symmetry, *Phys. Rev. Lett.* **100**, 013904 (2008).
- [3] T. Ozawa, H. M. Price, A. Amo, N. Goldman, M. Hafezi, L. Lu, M. C. Rechtsman, D. Schuster, J. Simon, O. Zilberberg, and I. Carusotto, Topological photonics, *Rev. Mod. Phys.* **91**, 015006 (2019).
- [4] Z. Wang, Y. Chong, J. D. Joannopoulos, and M. Soljacic, Observation of unidirectional backscattering-immune topological electromagnetic states, *Nature* **461**, 772 (2009).
- [5] L. Feng, R. El-Ganainy, and L. Ge, Non-Hermitian photonics based on parity-time symmetry, *Nat. Photonics* **11**, 752 (2017).
- [6] Z. Lin, H. Ramezani, T. Eichelkraut, T. Kottos, H. Cao, and D. N. Christodoulides, Unidirectional Invisibility Induced by PT-Symmetric Periodic Structures, *Phys. Rev. Lett.* **106**, 213901 (2011).
- [7] P. Miao, Z. Zhang, J. Sun, W. Walasik, S. Longhi, N. M. Litchinitser, and L. Feng, Orbital angular momentum microlaser, *Science* **353**, 464 (2016).
- [8] L. D. Barron, *Molecular Light Scattering and Optical Activity* (Cambridge University Press, Cambridge, 2004).
- [9] J. T. Collins, C. Kuppe, D. C. Hooper, C. Sibilia, M. Centini, and V. K. Valev, Chirality and chiroptical effects in metal nanostructures: Fundamentals and current trends, *Adv. Opt. Mater.* **5**, 1700182 (2017).
- [10] J. Mun, M. Kim, Y. Yang, T. Badloe, J. Ni, Y. Chen, C.-W. Qiu, and J. Rho, Electromagnetic chirality: From fundamentals to nontraditional chiroptical phenomena, *Light Sci. Appl.* **9**, 139 (2020).
- [11] X. Mu, L. Hub, Y. Cheng, Y. Fangc, and M. Suna, Chiral surface plasmon enhanced chiral spectroscopy: Principles and applications, *Nanoscale* **13**, 581 (2021).
- [12] A. O. Govorov, Z. Fan, P. Hernandez, J. M. Slocik, and R. R. Naik, Theory of circular dichroism of nanomaterials comprising chiral molecules and nanocrystals: Plasmon enhancement, dipole interactions, and dielectric effects, *Nano Lett.* **10**, 1374 (2010).
- [13] W. Liu, Z. Zhu, K. Deng, Z. Li, Y. Zhou, H. Qiu, Y. Gao, S. Che, and Z. Tang, Gold nanorod@chiral mesoporous silica core-shell nanoparticles with unique optical properties, *J. Am. Chem. Soc.* **135**, 9659 (2013).
- [14] N. A. Abdulrahman, Z. Fan, T. Tonooka, S. M. Kelly, N. Gadegaard, E. Hendry, A. O. Govorov, and M. Kadodwala, Induced chirality through electromagnetic coupling between chiral molecular layers and plasmonic nanostructures, *Nano Lett.* **12**, 977 (2012).
- [15] M. L. Nesterov, X. Yin, M. Schaferling, H. Giessen, and T. Weiss, The role of plasmon-generated near fields for enhanced circular dichroism spectroscopy, *ACS Photonics* **3**, 578 (2016).
- [16] D. M. Lipkin, Existence of a new conservation law in electromagnetic theory, *J. Math. Phys. (N.Y.)* **5**, 696 (1964).
- [17] J. E. Vázquez-Lozano and A. Martínez, Optical Chirality in Dispersive and Lossy Media, *Phys. Rev. Lett.* **121**, 043901 (2018).
- [18] Y. Tang and A. E. Cohen, Optical Chirality and Its Interaction with Matter, *Phys. Rev. Lett.* **104**, 163901 (2010).

- [19] Y. Tang and A. E. Cohen, Enhanced enantioselectivity in excitation of chiral molecules by superchiral light, *Science* **332**, 333 (2011).
- [20] E. Hendry, R. V. Mikhaylovskiy, L. D. Barron, M. Kadodwala, and T. J. Davis, Chiral electromagnetic fields generated by arrays of nanoslits, *Nano Lett.* **12**, 3640 (2012).
- [21] E. Hendry, T. Carpy, J. Johnston, M. Popland, R. V. Mikhaylovskiy, A. J. Laphorn, S. M. Kelly, L. D. Barron, N. Gadegaard, and M. Kadodwala, Ultrasensitive detection and characterization of biomolecules using superchiral fields, *Nat. Nanotechnol.* **5**, 783 (2010).
- [22] M. Schaferling, D. Dregely, M. Hentschel, and H. Giessen, Tailoring Enhanced Optical Chirality: Design Principles for Chiral Plasmonic Nanostructures, *Phys. Rev. X* **2**, 031010 (2012).
- [23] E. Petronijevic, E. M. Sandoval, M. Ramezani, C. L. Ordonez-Romero, C. Noguez, F. A. Bovino, C. Sabilia, and G. Pirruccio, Extended chiro-optical near-field response of achiral plasmonic lattices, *J. Phys. Chem. C* **123**, 23620 (2019).
- [24] T. Stauber, T. Low, and G. Gómez-Santos, Plasmon-enhanced near-field chirality in twisted van der Waals heterostructures, *Nano Lett.* **20**, 8711 (2020).
- [25] C. S. Ho, A. Garcia-Etxarri, Y. Zhao, and J. Dionne, Enhancing enantioselective absorption using dielectric nanospheres, *ACS Photonics* **4**, 197 (2017).
- [26] K. Yao and Y. Zheng, Near-ultraviolet dielectric metasurfaces: From surface-enhanced circular dichroism spectroscopy to polarization-preserving mirrors, *J. Phys. Chem. C* **123**, 11814 (2019).
- [27] E. Mohammadi, A. Tavakoli, P. Dehkhoda, Y. Jahani, K. L. Tsakmakidis, A. Titt, and H. Altug, Accessible superchiral near-fields driven by tailored electric and magnetic resonances in all-dielectric nanostructures, *ACS Photonics* **6**, 1939 (2019).
- [28] J. García-Guirado, M. Svedendahl, J. Puigdollers, and R. Quidant, Enhanced chiral sensing with dielectric nanoresonators, *Nano Lett.* **20**, 585 (2020).
- [29] H. Rhee, Y. G. June, J. S. Lee, K. K. Lee, J. H. Ha, Z. H. Kim, S. J. Jeon, and M. Cho, Femtosecond characterization of vibrational optical activity of chiral molecules, *Nature* **458**, 310 (2009).
- [30] M. H. M. Janssen and I. Powis, Detecting chirality in molecules by imaging photoelectron circular dichroism, *Phys. Chem. Chem. Phys.* **16**, 856 (2014).
- [31] S. Beaulieu, A. Comby, D. Descamps, B. Fabre, G. A. Garcia, R. Géneaux, A. G. Harvey, F. Légaré, Z. Mašín, L. Nahon, A. F. Ordonez, S. Petit, B. Pons, Y. Mairesse, O. Smirnova, and V. Blanchet, Photoexcitation circular dichroism in chiral molecules, *Nat. Phys.* **14**, 484 (2018).
- [32] D. Sofikitis, L. Bougas, G. E. Katsoprinakis, A. K. Spiliotis, B. Loppinet, and T. P. Rakitzis, Evanescent-wave and ambient chiral sensing by signal-reversing cavity ringdown polarimetry, *Nature* **514**, 76 (2014).
- [33] M. Tulio, S. Rosado, M. Leonor, R. S. Duarte, and R. Fausto, Vibrational spectra (FT-IR, Raman and MI-IR) of  $\alpha$ - and  $\beta$ -alanine, *J. Mol. Struct.* **343**, 410 (1997).
- [34] S. Jähnigen, A. Scherrer, R. Vuilleumier, and D. Sebastiani, Chiral crystal packing induces enhancement of vibrational circular dichroism, *Angew. Chem. Int. Ed.* **57**, 3344 (2018).
- [35] F. J. Rodríguez-Fortuño, G. Marino, P. Ginzburg, D. O'Connor, A. Martínez, G. A. Wurtz, and A. V. Zayats, Near-field interference for the unidirectional excitation of electromagnetic guided modes, *Science* **340**, 328 (2013).
- [36] F. J. Garcia de Abajo, Optical excitations in electron microscopy, *Rev. Mod. Phys.* **82**, 211 (2010).
- [37] A. Ciattoni, C. Conti, A. V. Zayats, and A. Marini, Electric control of spin-orbit coupling in graphene-based nanostructures with broken rotational symmetry, *Laser Photonics Rev.* **14**, 2000214 (2020).
- [38] A. Ciattoni, C. Conti, and A. Marini, Electric Directional Steering of Cathodoluminescence From Graphene-Based Hybrid Nanostructures, *Phys. Rev. Appl.* **15**, 054016 (2021).
- [39] N. Meinzer, E. Hendry, and W. L. Barnes, Probing the chiral nature of electromagnetic fields surrounding plasmonic nanostructures, *Phys. Rev. B* **88**, 041407(R) (2013).
- [40] M. Cotrufo, C. I. Osorio, and A. F. Koenderink, Spin-dependent emission from arrays of planar chiral nanoantennas due to lattice and localized plasmon resonances, *ACS Nano* **10**, 3389 (2016).
- [41] L. V. Poulikakos, P. Gutsche, K. M. McPeak, S. Burger, J. Niegemann, C. Hafner, and D. J. Norris, Optical chirality flux as a useful far-field probe of chiral near fields, *ACS Photonics* **3**, 1619 (2016).
- [42] L. V. Poulikakos, P. Thureja, A. Stollmann, E. De Leo, and D. J. Norris, Chiral light design and detection inspired by optical antenna theory, *Nano Lett.* **18**, 4633 (2018).
- [43] A. Ciattoni, C. Conti, and A. Marini, Multipolar terahertz absorption spectroscopy ignited by graphene plasmons, *Commun. Phys.* **2**, 111 (2019).
- [44] A. O. Govorov and Z. Fan, Theory of chiral plasmonic nanostructures comprising metal nanocrystals and chiral molecular media, *ChemPhysChem* **13**, 2551 (2012).
- [45] J. Schwinger, L. L. Deraad Jr., K. A. Milton, W. Tsai, and J. Norton, *Classical Electrodynamics* (CRC Press, Boca Raton, 1998), 1st ed.
- [46] C. F. Chen, C. H. Park, B. W. Boudouris, J. Horng, B. Geng, C. G. Girit, A. Zettl, M. F. Crommie, R. A. Segalman, S. G. Louie, and F. Wang, Controlling inelastic light scattering quantum pathways in graphene, *Nature* **471**, 617 (2011).
- [47] H. Liu, Y. Liu, and D. Zhu, Chemical doping of graphene, *J. Mater. Chem.* **21**, 3335 (2011).
- [48] E. H. Hwang and S. Das Sarma, Dielectric function, screening, and plasmons in two-dimensional graphene, *Phys. Rev. B* **75**, 205418 (2007).
- [49] F. J. García de Abajo, Graphene plasmonics: Challenges and opportunities, *ACS Photonics* **1**, 135 (2014).